

Happy Catastrophe: recent progress in analysis and exploitation of elastic instability

A. R. Champneys¹, T. J. Dodwell^{2,3}, R. M. J. Groh¹, G. W. Hunt⁴, R. M. Neville¹,
A. Pirrera¹, A. H. Sakhaei², M. Schenk¹, M. A. Wade⁵.

¹*Faculty of Engineering, University of Bristol, Bristol, UK.*

²*College of Engineering, Mathematics & Physical Sciences, University of Exeter, Exeter, UK.*

³*The Alan Turing Institute, London, NW1 2DB, UK*

⁴*Department of Mechanical Engineering, University of Bath, Bath, UK.*

⁵*Department of Civil and Environmental Engineering, Imperial College London, London, UK.*

Correspondence*:
Prof. Giles Hunt
ensgwh@bath.ac.uk

2 ABSTRACT

3 A synthesis of recent progress is presented on a topic that lies at the heart of both structural
4 engineering and nonlinear science. The emphasis is on thin elastic structures that lose stability
5 subcritically — without a nearby stable post-buckled state — a canonical example being a
6 uniformly axially-loaded cylindrical shell. Such structures are hard to design and certify because
7 imperfections or shocks trigger buckling at loads well below the threshold of linear stability. A
8 resurgence of interest in structural instability phenomena suggests practical stability assessments
9 require stochastic approaches and imperfection maps. This article surveys a different philosophy;
10 the buckling process and ultimate post-buckled state are well described by the perfect problem.
11 The significance of the Maxwell load is emphasised, where energy of the unbuckled and fully-
12 developed buckle patterns are equal, as is the energetic preference of localised states, stable
13 and unstable versions of which connect in a snaking load-deflection path.

14 The state of the art is presented on analytical, numerical and experimental methods. Pseudo-
15 arclength continuation (path-following) of a finite-element approximation computes families of
16 complex localised states. Numerical implementation of a mountain-pass energy method then
17 predicts the energy barrier through which the buckling process occurs. Recent developments also
18 indicate how such procedures can be replicated experimentally; unstable states being accessed
19 by careful control of constraints, and stability margins assessed by shock sensitivity experiments.

20 Finally, the fact that subcritical instabilities can be robust, not being undone by reversal of the
21 loading path, opens up potential for technological exploitation. Several examples at different length
22 scales are discussed; a cable-stayed prestressed column, two examples of adaptive structures
23 inspired by morphing aeroelastic surfaces, and a model for a functional auxetic material.

24

25 **Keywords:** instability, elastic, buckling, sub-critical, localisation, path-following, mountain-pass

1 INTRODUCTION

26 Bernard Budiansky famously used to say “everybody loves a buckling problem” [1, 2] and this resonates
27 today in a number of significant ways. First, it reflects that buckling is a process of instability, and
28 instabilities have always held a macabre fascination for children and adults alike. From the collapse of a
29 pile of bricks to the deliberate demolition of buildings or the catastrophic failures of large urban areas in
30 the aftermath of a natural disaster, instabilities hold a central place in human experience and consciousness.
31 But there is a newer, more modern, context — that structural instabilities can also be harnessed for the
32 greater good. See, for example, the recent paper by Pedro Reis [3] who coined the phrase *buckliphilia* for
33 the exploitation of instability in counterpoint to *buckliphobia*, the safety-conscious avoidance of collapse.

34 The purpose here is to review modern developments in the theory and analysis of buckling instabilities,
35 both in the work of the present authors and by others. In the process, we draw particular attention to new
36 techniques of analysis — often applied to classical thorny buckliphobic problems — and highlight potential
37 areas of buckliphilic exploitation. We place particular emphasis on the interplay between analytical,
38 numerical and experimental techniques, showing how we pick our way through a plethora of unstable
39 post-buckling equilibrium states, to focus on practically relevant solutions.

40 With its origins in singularity, or catastrophe, theory [4, 5], the nonlinear analysis of structural buckling
41 can be cast in the framework of static bifurcation theory. Broadly speaking, the instability of a trivial,
42 unbuckled state, upon varying an external load parameter, falls into one of three categories: supercritical,
43 subcritical or transcritical; see Figure 1. The former is sometimes called a *safe* bifurcation because, as
44 shown in panel (a), the post-buckled path emerges smoothly out of the unbuckled equilibrium path, and
45 hence stability can be safely tracked under slow variation of the applied load. In contrast, subcritical
46 bifurcations, **as seen in panel (b)**, have been termed *dangerous* [6], because the structure would irreversibly
47 jump to a post-buckled state (**not shown**) that is a long way from the trivial one. Such jumps in elastic
48 structures tend to give rise to energy loss, accompanied by a significant “bang”, and often lead to permanent
49 non-elastic deformation or collapse. Transcritical instabilities (c) lie somewhere in between and are often
50 associated with a loss of reflection symmetry. There is an extensive literature on understanding and
51 classifying buckling instabilities, see for example Thompson & Hunt [7] and references therein. This paper
52 shall concern instabilities that lead to large irreversible jumps.

53 Subcritical bifurcations, exemplified by the classic responses of thin elastic shells, are known to carry
54 distinctive features such as the likelihood of extreme imperfection-sensitivity and wide experimental scatter,
55 and certainly merit a general overview. The canonical example is that of the axially-loaded cylindrical
56 shell, of interest to rocket designers, aircraft and storage tank manufacturers, as well as in the construction
57 of buffers to absorb mechanical energy. Here, instability under realistic conditions occurs significantly
58 below the critical load of the system as determined from linear stability analysis of the perfect problem,
59 absent from imperfections.

60 One approach to deal with such imperfection-sensitivity is through stochastic methods. Eliashakoff,
61 Arbocz and others pioneered developments such as the international databank of imperfections, see [8, 9]
62 and references therein. While such methods appeal at one level, from a modelling point of view there is also
63 significant sensitivity to the precision of the chosen numerical method, and useful analyses typically require
64 many Monte Carlo realisations. Also, from a practical perspective, estimating a safety margin of a particular
65 specimen would necessitate comprehensive imaging and analysis of all its imperfections. Unfortunately for
66 modern, lightweight composite structures, such imperfections often occur beneath the surface layer and are
67 hard to characterise in practice. There has therefore long been a search for a lower-bound criterion below

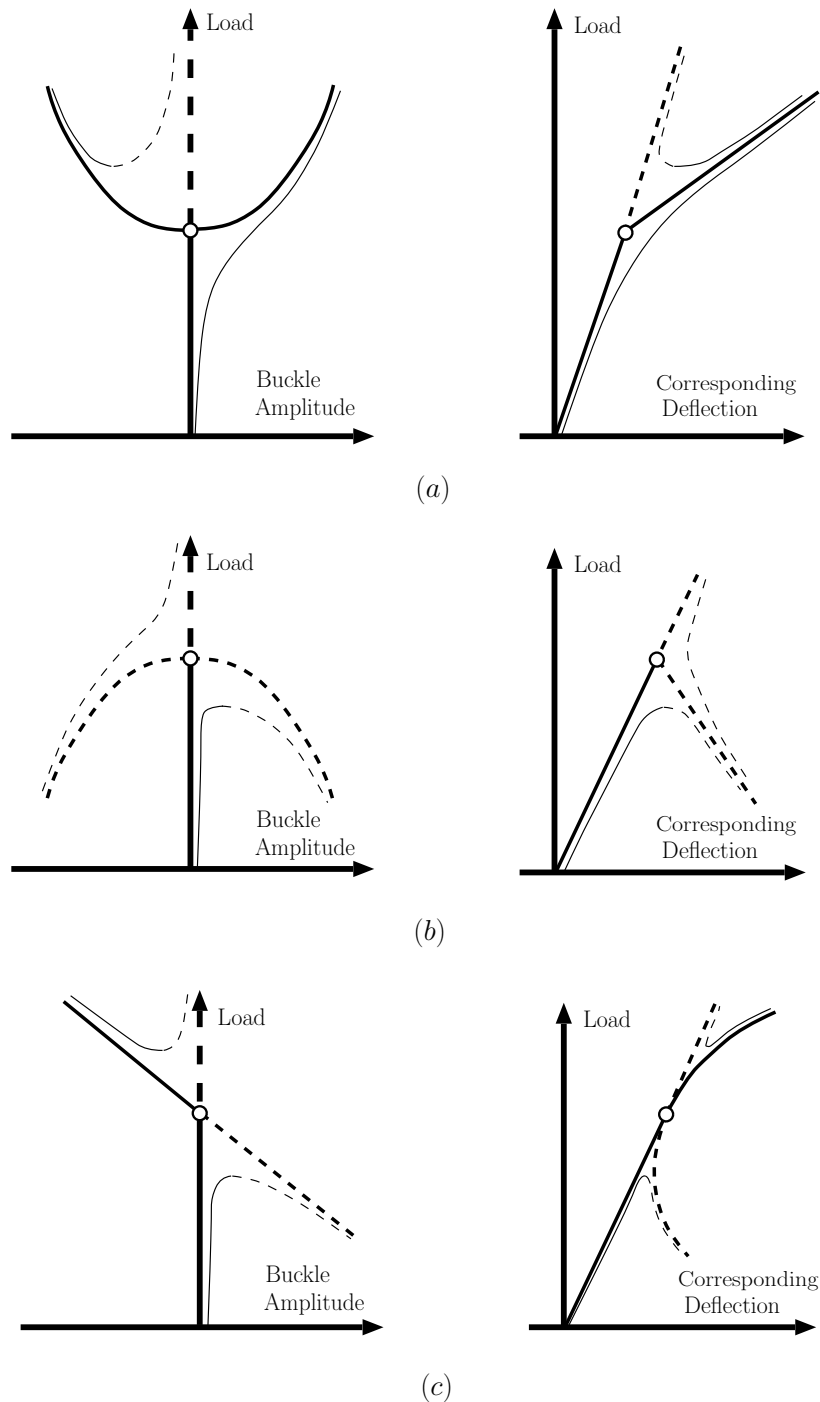


Figure 1. (a) Supercritical, (b) subcritical and (c) transcritical buckling instabilities and their unfolding in the presence of small symmetry-breaking effects. Heavy lines: perfect system. Light lines: imperfect system. Solid lines: stable. Broken lines: unstable **under controlled load**.

68 which a violently subcritical structure such as a cylindrical shell cannot buckle. One such phenomenological
 69 idea is that of a “reduced stiffness” approach [10], but such simple design formulae still require a full
 70 understanding of the nonlinear elastic equilibrium states of the shell.

71 Methods based on sensitivity to perturbations have received a recent resurgence of interest inspired by
 72 theories of critical transitions in fluid dynamics, see for example [11, 12]. The focus in these works is

73 sensitivity not to imperfection but to dynamic shocks; how large a dynamic perturbation in the form of a
74 small tap or localised impact would be needed to induce buckling. It is not clear yet whether such ideas
75 represent a realistic prospect for a practical non-destructive test for a particular specimen. Nevertheless, we
76 shall argue in Sec. 5 below that small localised *shocks* can allow engineers to explore the critical *mountain*
77 *pass* unstable equilibrium that provides the route to buckling.

78 Fundamentally, this paper takes a deterministic rather than stochastic point of view. Starting with the
79 perturbation methods introduced by the Dutch engineer Koiter [13], there is a rich tradition of using pseudo
80 arc-length continuation to track unstable post-buckling solutions emerging from classical bifurcation points
81 [14, 15, 16, 17, 18]. Supplemented by energy landscape considerations providing information on stability,
82 these methods can be interpreted fundamentally as implicit analytical approaches to studying equilibrium
83 solutions and their buckling paths. On the other hand, stochastic formulations, primarily explicit, after the
84 introduction of quasi-realistic imperfection types and shapes and often employing Monte Carlo techniques,
85 can be used to track expected dynamical behaviour for particular specimens (see *e.g.* [19, 20]). Clearly,
86 both approaches carry inherent advantages and disadvantages, and should be regarded as complementary.

87 A key idea is that the perfect problem, devoid of imperfections or shocks, can give theoretical and practical
88 insight into how structures buckle subcritically. We shall **emphasise the significance of the Maxwell load**,
89 the level at the fundamental and periodic buckle patterns have the same energy; see *e.g.* [21] and Sec. 4
90 below. Nearby spatially localised equilibria are energetically preferable. But to find such states, we need to
91 overcome an energy barrier, in the form of snaking or concertina pattern of unstable states connected by
92 sequences of folds. Numerically, these patterns can be captured using pseudo-arclength continuation, going
93 back to Riks [22]. But how can we embed such a methodology in modern finite-element analyses? How
94 can one access such unstable paths in an experiment? What is the best approach to understanding energy
95 barriers? These are the questions this paper seeks to answer. We shall also keep in mind the perspective
96 [3] that buckling instabilities, rather than to be avoided at all costs, can, in principle, be beneficial *happy*
97 *catastrophes*.

98 The rest of this paper is outlined as follows. Section 2 gives a brief overview of nonlinear post-buckling
99 analysis of subcritical problems, starting from the pivotal work of Koiter, and including some general
100 comments on analytical perturbation methods. A motivating simple pin-jointed “knee” model is presented
101 as well as the classical problem of the axially loaded cylindrical shell. Section 3 surveys recent progress in
102 computational path-following methods applied directly to a finite element representation to compute stable
103 and unstable paths, with illustrations for a simple snap-through structure as well as the more complex
104 cylindrical shell. Section 4 then considers computational energy-based methods that are able to identify
105 Maxwell loads and mountain-pass solutions, again with reference to the cylindrical shell. Section 5
106 considers emerging experimental ideas to implement the numerical methods from the previous sections,
107 via carefully controlled laboratory procedures. Section 6 surveys three examples, at different length-scales
108 and from distinct engineering domains, that attempt to exploit subcritical buckling instabilities: prestressed
109 stayed columns, adaptive aeroelastic structures, and a structural model for auxetic materials. Finally, Sec. 7
110 draws conclusions and suggests avenues for future work.

2 LARGE AMPLITUDE POST-BUCKLING ANALYSIS

111 Before the advent of modern computer-based methods, nonlinear post-buckling of elastic structures
112 was largely dealt with by systematic asymptotic analysis; *i.e.* perturbation procedures based on Taylor

113 expansions about the critical bifurcation point [7, 23]. The pioneer of this field was Warner T. Koiter (1914–
 114 1997), beginning with his PhD thesis, completed during the Second World War [13]. Local perturbation
 115 analysis can be highly instructive in highlighting fundamental properties like underlying symmetries and
 116 symmetry-breaking, yet its range of validity typically is limited. This observation is by no means new.
 117 Koiter, for example, in discussing the buckling of a spherical shell under external pressure in 1969 [24],
 118 states:

119 “In the problem of the spherical shell under external pressure the systematic perturbation procedure is
 120 only valid in a range of load factors within a fraction of the order h/R of the critical load, and for
 121 deflections of the order $(h/R)^{1/2}$ times the shell thickness. It follows that the systematic perturbation
 122 procedure at the critical point has little, if any, practical significance for the present problem.”

123 Here h represents the shell thickness and R the radius. He went on to suggest the following:

124 “A far more powerful method of achieving a second approximation to the post-buckling behaviour
 125 was also developed already in our earlier work [13, section 38]. It consists of an evaluation of the
 126 quartic terms in the energy expression not at the critical load itself, but at the actual value of the load
 127 factor under consideration.”

128 The reference is of course to his thesis [13], which did not appear in English until 1967 and was never
 129 published in the open literature. Koiter was a deeply humble man.

130 In more recent years Koiter’s ideas have been supplemented by other asymptotic techniques,
 131 such as expansions at the so-called Maxwell load [25] and pseudo arc-length continuation which will be
 132 explained in Sec. 3 below. Throughout this article we will apply our ideas to the recurring infinite-degree-
 133 of-freedom example of the axially-compressed cylindrical shell. But first, let us introduce a simple single
 134 degree-of-freedom example.

135 2.1 A simple motivating example

136 Consider the simple mechanical model of Fig. 2. A linear spring k is placed in-line with a “knee”
 137 comprising two finite-length rigid links hinged with a rotational spring, and compressed by an axial force
 138 P as shown. The rotational spring can take various characteristics — elastic, rigid-plastic or elasto-plastic,
 139 as shown in the insets. **It is also assumed that the arms can pass through one another without restriction.**

140 The system has two degrees-of-freedom, with associated generalised coordinates Δ and θ that respectively
 141 describe in-line displacement and rotation of the rigid link elements. It has three distinct possibilities for
 142 equilibrium. First, we have the simplest state in which the rotational spring does no work and the in-line
 143 spring simply squashes to give a *fundamental equilibrium path* describing the pre-buckling state:

$$P = k\Delta. \quad (1)$$

144 Second, under the condition that the knee rotation θ continues to grow in the positive sense, the potential
 145 energy function for the post-buckling response is either

$$V = \frac{1}{2}K(2\theta)^2 + \frac{1}{2}k[\Delta - L(1 - \cos\theta)]^2 - P\Delta,$$

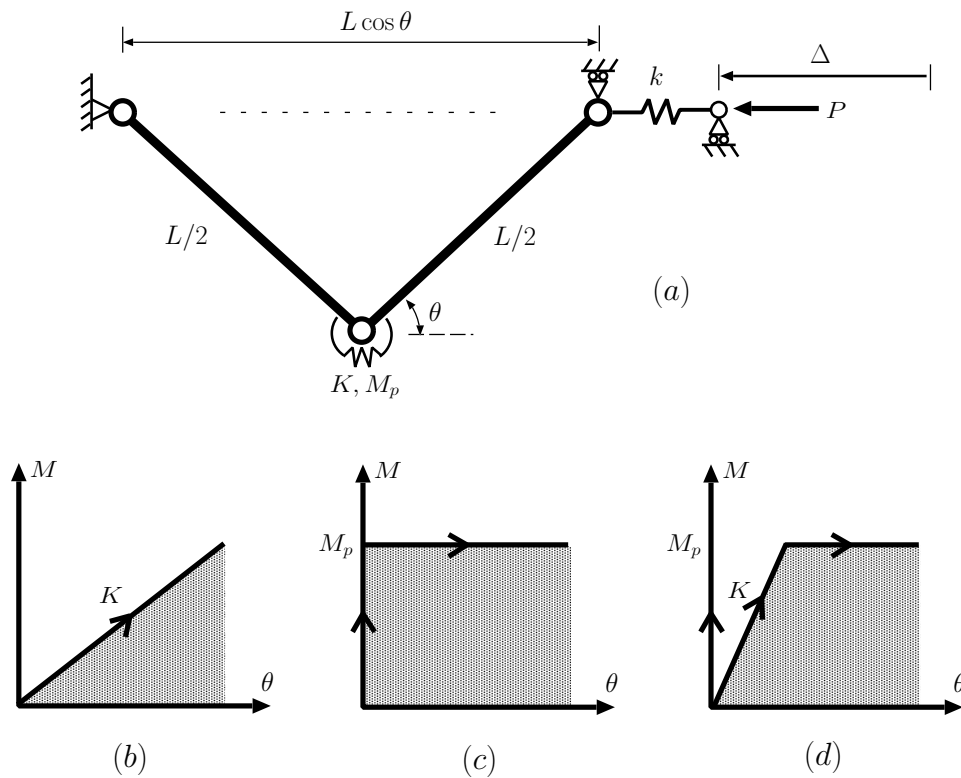


Figure 2. (a) Schematic of a simple knee model. (b)-(d) Load-deflection diagrams for the case of (b) an elastic rotational spring, (c) rigid-plastic rotational spring and (d) elasto-plastic rotational spring.

146 when the rotational spring is elastic with rotational stiffness K , or

$$V = 2M_p\theta + \frac{1}{2}k[\Delta - L(1 - \cos\theta)]^2 - P\Delta,$$

147 if it has passed its limiting plastic moment M_p . In each case, the first two terms are the strain energies in
 148 the rotational and in-line springs respectively; the final subtracted term is the work done by the dead load
 149 P . When the rotational spring is in the plastic state, its energy contribution can be seen as *quasi-strain*
 150 *energy*, i.e. the work done in moving the joint through positive rotation, without necessarily being able to
 151 release this work if the rotation is reversed. Responses are then readily obtained in closed form from the
 152 two equilibrium equations $\partial V/\partial\theta = 0$ and $\partial V/\partial\Delta = 0$.

153 The fundamental and post-buckling paths are plotted in Fig. 3 for the three possibilities of Fig. 2. There are
 154 several points worthy of note. For the elastic system of Fig. 2(a) the initially-stable pure-squash fundamental
 155 equilibrium state reaches a supercritical bifurcation point B where it becomes unstable, whereupon one
 156 branch of the stable post-buckling path is then followed. Post-buckling analysis of this type of behaviour
 157 responds well to the perturbation method [7].

158 The rigid-plastic system on the other hand has no bifurcation point, and this highlights one of the key
 159 issues to be addressed in this paper. Over much of the range, the fundamental and post-buckling paths,
 160 although being relatively well-separated in the $P - \theta$ plot, lie close to one another in the $P - \Delta$ diagram.
 161 Moreover, although the paths approach each other asymptotically, they never meet; the bifurcation exists
 162 only at infinite load. Yet when the load is high, buckling could certainly be triggered by small imperfections
 163 or fluctuations. So the real problem becomes to determine a practical range of loads over which the system

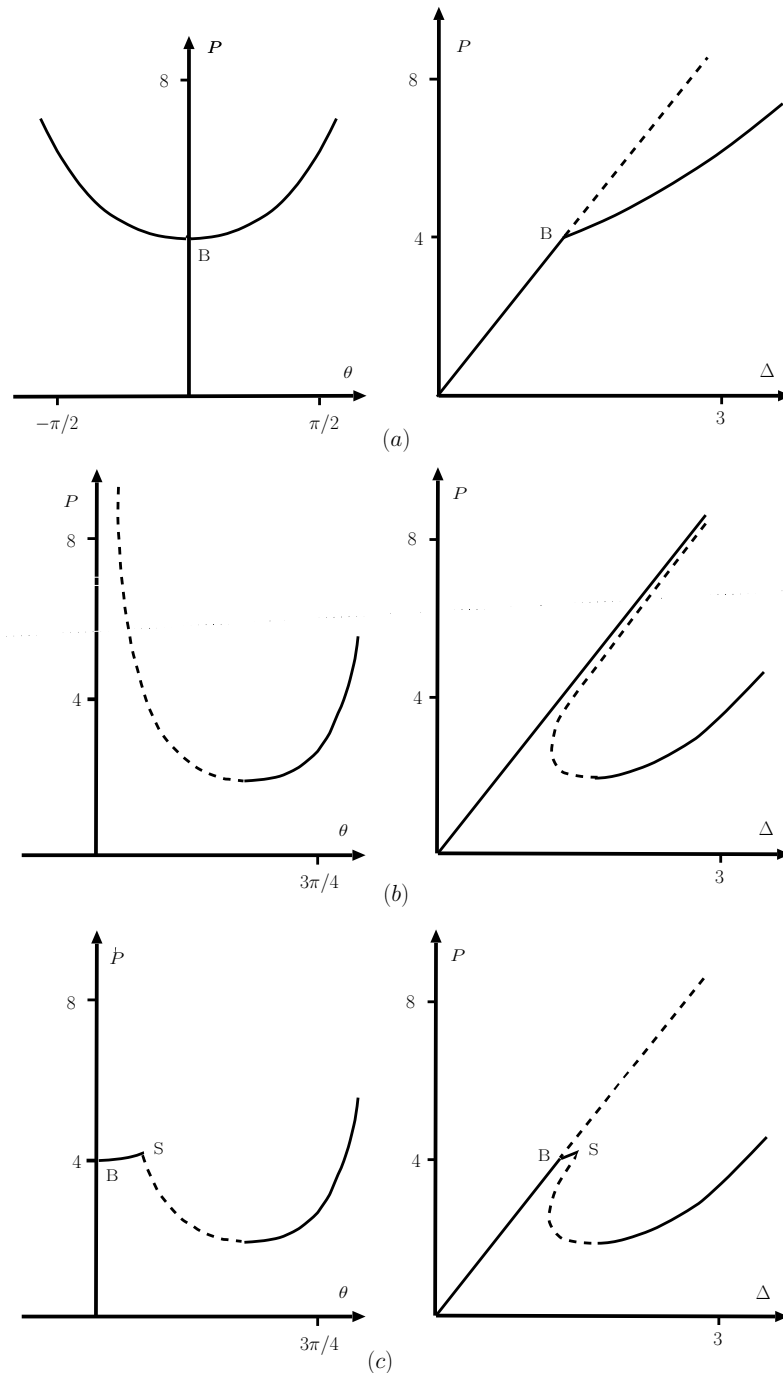


Figure 3. Responses of the knee models of Fig. 2 for the parameter values $L = 1$, $k = 3$, $K = 1$ and $M_p = 1$. Left: load versus θ . Right: load versus end-shortening. (a) Elastic joint of Fig. 2(b). (b) Rigid-plastic joint of Fig. 2(c). (c) Elasto-plastic joint of Fig. 2(d). Unstable paths under controlled load are shown as broken lines.

164 can be assumed to be relatively safe from instability. Another point to note in this case is that although
 165 the buckled path represents pure plastic behaviour with zero stiffness, there remains an effective stiffness
 166 on this path beyond its minimum load point, **once the arms have passed through vertical**. This stiffness
 167 is due to geometric effects (deflection perpendicular to the load remaining constrained). A number of
 168 circumstances are known where such geometrically-nonlinear, infinite-buckling-load problems arise in
 169 practice, for instance the buckling of railway tracks in heatwave conditions [26], and kink-banding of

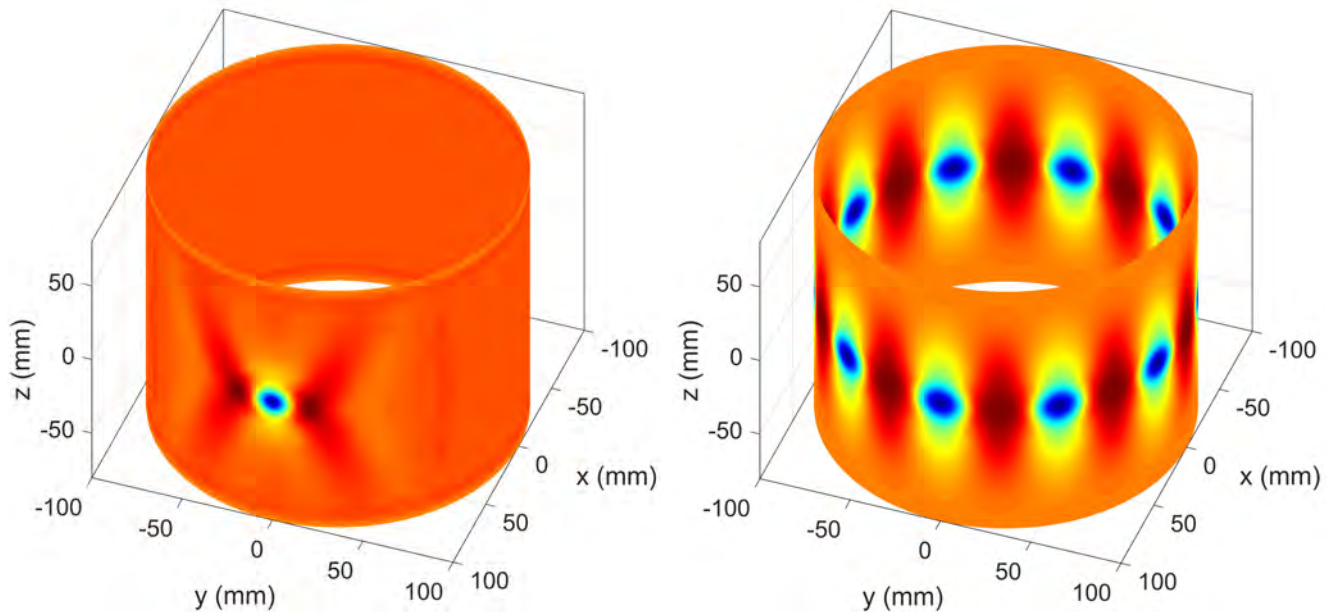


Figure 4. (a) An axially compressed cylinder features an unstable post-buckling equilibrium in the shape of a single inwards dimple, corresponding to the mountain-pass point between the stable pre-buckling and restabilised post-buckling regimes. (b) Through the process described in Section 3 the single dimple can multiply circumferentially to form a single row of axially-localised buckles.

170 layered materials [27]. A major theme here is to review techniques for obtaining ball-park estimates for
 171 effective buckling loads and post-buckling information for such problems.

172 The bifurcation point is restored for the elasto-plastic system as shown in the bottom row of panels
 173 in Fig. 3, where the behaviour follows the purely elastic response of the top panels until the rotational
 174 moment reaches its plastic limit, whereupon it switches to the rigid-plastic response of the middle row. The
 175 absence of a first bifurcation point is avoided, but an effective secondary bifurcation point \mathbf{S} also needs
 176 to be negotiated. As with many interactive buckling problems there is the danger that the continuation of
 177 the elastic path remains as a possible equilibrium solution. This simple example emphasises that modern
 178 path-following computational methods need to be constantly vigilant in checking for further instability
 179 points and bifurcations as they track along an equilibrium path.

180 2.2 The axially-compressed cylindrical shell

181 Much has been written on the classical problem of the buckling of an axially loaded cylindrical shell, see
 182 *e.g.* [28, 2] and references therein. It carries all the hallmarks of a classical subcritical buckling problem, in
 183 particular its notorious sensitivity to imperfections. Its apparent simplicity, yet underlying complexity, has
 184 ignited significant academic dueling over the course of the last century (cf. different “resolutions” of the
 185 “paradox” by Zhu et al. [29] and Elishakoff [30]), and caused design engineers many a headache.

186 It might seem strange in a forward-looking review paper to focus on such a problem, but with the modern
 187 impetus towards ever stronger and lighter structures and new materials, understanding the cylinder response
 188 remains a fundamental issue of continuing research. We will therefore use axially-compressed cylindrical
 189 shell buckling as the exemplar problem on which to illustrate the methodology reviewed in this paper.

190 When the fundamental deformation mode of a long, slender structure loses stability, it can either transition
 191 into a periodic buckling mode, spread equally over the domain, or a localised mode that is concentrated

192 only over a portion of the domain. Such different kinds of buckle patterns were illustrated in the beautiful
 193 experimental and computational work of Yamaki [31]. It is well known that localised post-buckling modes
 194 have a proclivity to develop in systems governed by subcritical bifurcations [32]. Moreover, Hunt and
 195 Lucena Neto [33] showed that axially localised post-buckling modes exist for the axially compressed
 196 cylinder. This circumferential ring of an axially localised, diamond-shaped waveform can then undergo
 197 homoclinic snaking in the compressive loading parameter, leading to sequential ring formation along the
 198 length of the cylinder [34].

199 The work by Horák *et al.* [35] showed that an unstable equilibrium — localised axially and
 200 circumferentially — in the form of a single dimple is also possible (see Figure 4(a)). This state corresponds
 201 to the mountain-pass solution separating the stable pre-buckling and restabilised post-buckled states.
 202 The initial dimple, which can be found using the mountain pass algorithm of Sec. 4, can undergo
 203 circumferential snaking, culminating in one ring of diamond-shaped buckles (see Figure 4(b)). This
 204 type of circumferentially-driven snaking is different from the axially-driven snaking described by Hunt *et*
 205 *al.* [34], where circumferentially-complete rings of buckles grow axially in a sequential manner.

206 We shall continually return to the squashed cylinder problem throughout this study.

207 **2.3 Post-buckling analysis — a post-Koiter reflection**

208 Another canonical shell buckling problem that has received a resurgence of interest due to the recent
 209 work of Hutchinson [36] is that of the spherical shell under uniform external pressure. That problem too
 210 exhibits violently subcritical bifurcation and shock-sensitivity. In an extended paper published in 1969
 211 Koiter [24] writes

212 “An important result of Beaty’s analysis [37] was that the numerical factor of the quartic term is
 213 much larger than the coefficient of the cubic term, indicating that the quartic term becomes already
 214 important for very small deflections in terms of the shell thickness, and that it is dominant over the
 215 cubic term for larger deflections. A similar evaluation of the quartic term in the energy expression
 216 at the critical load factor and for rotationally symmetric deformations was made independently by
 217 Walker [38], who also evaluated the next higher-order term, namely the quintic term, with an even
 218 larger numerical coefficient.”

219 He thus puts the poor performance of the perturbation method down to ever increasing influence of
 220 higher and higher-order terms — quartics larger than cubics, quintics more than quartics, and so on. This
 221 significant observation seems odd from the viewpoint of perturbation theory; using von Kármán–Donnell
 222 equations for the cylindrical shell [39] for example, a discrete formulation comprising doubly-periodic
 223 shapes generates energy terms only up to quartic level [7].

224 The need for higher-order terms can be explained through the process of *elimination of passive*
 225 *coordinates*, as espoused in the book by Thompson and Hunt [7]. Consider a conservative elastic structural
 226 system whose stable equilibrium configurations are described by minima of the energy function $W(q_i, \Lambda)$,
 227 where $\{q_i\}$ describes a set of n incremental generalised coordinates measured from a monotonically-
 228 increasing (fundamental) equilibrium path in loading parameter Λ . Suppose that $n - m$ of the q_i are deemed
 229 *passive* (not actively involved in the buckling process). These passive terms are represented parametrically
 230 in terms of the remaining m *active* coordinates and loading parameter thus, $q_\alpha = q_\alpha(q_j, \Lambda)$, where now
 231 $1 \leq j \leq m$ and $m + 1 \leq \alpha \leq n$. A new energy function $\mathcal{W}(q_j, \Lambda)$, equal in value to the W -function, but

232 written in terms of just the active coordinates and loading parameter, is introduced:

$$\mathcal{W}(q_i, \Lambda) \equiv W[q_j, q_\alpha(q_j, \Lambda), \Lambda]. \quad (2)$$

233 Differentiation using the chain rule then gives derivatives of \mathcal{W} in terms of W . Specifically, if W is
 234 diagonalised such that $W_{ij} = 0$ for $i \neq j$, subscripts denoting partial differentiation with respect to the
 235 appropriate generalised coordinate, then derivatives up to cubic level pass over unchanged, but at quartic
 236 level we see contamination from lower-order derivatives. In particular,

$$\mathcal{W}_{1111} = W_{1111} - 3 \sum_{\alpha=m+1}^n \frac{W_{\alpha 11}^2}{W_{\alpha\alpha}} \quad (3)$$

237 for a significant quartic term (see [7] for more details). Similar contamination from lower derivatives
 238 likewise appears at quintic level and above, leading to a lack of convergence as described in the Koiter
 239 quote above.

240 The derivative $W_{\alpha\alpha}$ appearing in the denominator of (3) is the so-called *stability coefficient* for the
 241 passive coordinate q_α , and would have equated to zero had the coordinate been active and directly involved
 242 in the buckling process. If critical loads tend to bunch together on the fundamental path, as occurs for
 243 both the axially-compressed cylinder and pressurised sphere discussed above, then contamination from
 244 higher-modes close to the critical point of interest can clearly be extreme.

245 Modal analysis in the form of spectral or pseudo-spectral numerical methods made a resurgence in
 246 the 1990s and 2000s, allowing numerical continuation (path-following) methods to scale to models with
 247 hundreds of degrees-of-freedom (see e.g. [21, 40]). Nowadays, with modern computers being able to cope
 248 easily with millions of degrees-of-freedom, because of its geometric versatility the finite element method is
 249 the preferred technique for solving complex problems in engineering mechanics. Results provided in the
 250 next section are therefore presented in a finite-element setting.

3 NUMERICAL PATH-FOLLOWING FOR SUBCRITICAL INSTABILITIES

251 In applied mathematics, methods for multi-parameter analysis, branch-switching and bifurcation tracking
 252 are well established theoretically using the language of catastrophe (singularity) theory [41] and
 253 differentiable dynamical systems, see [42], including in infinite dimensions [43]. Using the concept
 254 of pseudo-arclength continuation due to Keller [44] these methods have been implemented numerically
 255 and incorporated into a variety of numerical continuation software packages, such as AUTO [45]. Typically
 256 such formulations apply to systems governed by ordinary or partial differential equations. In structural
 257 mechanics, specialised arc-length techniques were developed for nonlinear formulations by Riks [14] and
 258 Crisfield [15]. Classically, those studies tended to be restricted to a single parameter — the applied load.
 259 However, the formulation can easily be extended to the general setting, as described here.

260 Our formulation considers a discretised model of a quasi-statically evolving, conservative and elastic
 261 structure, where the internal forces, $\mathbf{f}(\mathbf{u})$, and tangential stiffness, $\mathbf{K}_T(\mathbf{u})$, are uniquely defined from
 262 the current displacements, \mathbf{u} , by means of the first and second variations of the total potential energy.
 263 Here \mathbf{u} may represent all the degrees-of-freedom of a simple system, or a large-scale reduction of an
 264 infinite-dimensional problem. We first present a general framework, then illustrate the results for a simple
 265 toggle frame, before discussing implications for the cylindrical shell problem.

266 **3.1 The general setting**

267 Equilibrium is defined as a balance between internal and external forces acting on the structure. In
 268 a displacement-based finite element setting, this balance is written in terms of n discrete displacement
 269 degrees-of-freedom \mathbf{u} , and a scalar loading parameter λ :

$$\mathbf{F}(\mathbf{u}, \lambda) = \mathbf{f}(\mathbf{u}) - \mathbf{p}(\lambda) = \mathbf{0}. \tag{4}$$

270 The vectors $\mathbf{p}(\lambda)$ and $\mathbf{f}(\mathbf{u})$ are the external (non-follower) load and internal force, respectively. In the case
 271 of linear and proportional loading we have $\mathbf{p}(\lambda) \equiv \lambda \mathbf{p}_{,\lambda}^1 = \lambda \hat{\mathbf{p}}$, where $\hat{\mathbf{p}}$ is a constant reference loading
 272 vector (dead loading).

The system (4) of n equations in $(n + 1)$ unknowns — n displacement degrees-of-freedom and one loading parameter — is solved for a solution point,

$$\mathbf{x} = (\mathbf{u}, \lambda).$$

To turn this into a well-posed system of equations, one needs to add an additional scalar constraint, the most natural of which is the arclength constraint

$$N(\mathbf{x}) = \mathbf{n}_u^\top \mathbf{u} + n_\lambda \lambda - \sigma = 0.$$

273 Hence

$$\mathbf{F}^N(\mathbf{x}) \equiv \begin{pmatrix} \mathbf{F}(\mathbf{x}) \\ N(\mathbf{x}) \end{pmatrix} = \mathbf{0}, \tag{5}$$

where \mathbf{n}_u and n_λ take different forms depending on the nature of the arclength constraint. By linearising about the current equilibrium state, \mathbf{x} , and applying Newton’s method for the iterative correction, $\delta \mathbf{x}$,

$$\begin{aligned} \mathbf{F}^N(\mathbf{x} + \delta \mathbf{x}) &= \mathbf{F}^N(\mathbf{x}) + \mathbf{F}_{,\mathbf{x}}^N(\mathbf{x}) \delta \mathbf{x} + \mathcal{O}(\delta \mathbf{x}^2) \equiv \mathbf{0} \\ \Rightarrow \delta \mathbf{x} &= - \left(\mathbf{F}_{,\mathbf{x}}^N(\mathbf{x}) \right)^{-1} \mathbf{F}^N(\mathbf{x}), \end{aligned} \tag{6}$$

274 we can find a set of solution points describing a continuous equilibrium curve. Note that the partial
 275 derivative of the residual with respect to the displacement vector, $\mathbf{F}_{,\mathbf{u}} = \mathbf{f}_{,\mathbf{u}}(\mathbf{u})$, is equal to the tangential
 276 stiffness matrix $\mathbf{K}_T(\mathbf{u})$.

277 More generally, Eq. (4) can be adapted to incorporate any number of additional parameters:

$$\mathbf{F}(\mathbf{u}, \mathbf{\Lambda}) = \mathbf{f}(\mathbf{u}, \mathbf{\Lambda}_1) - \mathbf{p}(\mathbf{\Lambda}_2) = \mathbf{0}, \tag{7}$$

where

$$\mathbf{\Lambda} = [\mathbf{\Lambda}_1^\top, \mathbf{\Lambda}_2^\top]^\top = [\lambda_1, \dots, \lambda_p]^\top$$

278 is a vector containing p control variables. Typically, $\mathbf{\Lambda}_1$ corresponds to parameters that influence the
 279 internal forces (*e.g.* material properties, geometric dimensions, temperature and moisture fields) and $\mathbf{\Lambda}_2$
 280 relates to externally applied mechanical loads (*e.g.* forces, moments, tractions).

¹ The comma notation is used throughout to denote differentials with respect to subscripted variables.

281 The number n of equilibrium equations in Eq. (7), correspond directly to the n displacement degrees-
 282 of-freedom. Because the structural response is parametrised by p additional parameters, a p -dimensional
 283 solution manifold in $\mathbb{R}^{(n+p)}$ will be computed — the so-called *equilibrium hypersurface* [46]. By defining
 284 additional auxiliary equations, \mathbf{g} , specific solution subsets on this p -dimensional manifold are recovered. In
 285 the general setting we therefore find solutions to the augmented system

$$\mathbf{G}(\mathbf{u}, \Lambda) \equiv \begin{pmatrix} \mathbf{F}(\mathbf{u}, \Lambda) \\ \mathbf{g}(\mathbf{u}, \Lambda) \end{pmatrix} = \mathbf{0}. \quad (8)$$

286 When r auxiliary equations are defined, the solution to Eq. (8) is $(p - r)$ -dimensional. Hence, $r = p - 1$
 287 auxiliary equations are required to define a one-dimensional equilibrium curve in $\mathbb{R}^{(n+p)}$.

288 Posing the problem in this general manner allows the structural response to be viewed not only as a
 289 function of a varying load but also as a function of other parameters that define the structure. By treating
 290 these additional parameters as “forcing” variables in an arc-length solver, their effect on the structural
 291 response is readily obtained.

This general treatment naturally lends itself to the tracing of loci of singular points in parameter space. To constrain the system of n equilibrium equations to such a locus, we simultaneously enforce a criticality condition, for example,

$$\mathbf{K}_T \phi = \mathbf{0},$$

292 *i.e.* at least one eigenvector ϕ of the tangential stiffness matrix \mathbf{K}_T spans the nullspace. In the most general
 293 form, a vector of q auxiliary variables \mathbf{v} may be added to the auxiliary equations \mathbf{g} . Hence,

$$\mathbf{G}(\mathbf{u}, \Lambda, \mathbf{v}) \equiv \begin{pmatrix} \mathbf{F}(\mathbf{u}, \Lambda) \\ \mathbf{g}(\mathbf{u}, \Lambda, \mathbf{v}) \end{pmatrix} = \mathbf{0}. \quad (9)$$

Eq. (9) describes n equilibrium equations and r auxiliary equations in $(n + p + q)$ unknowns leading to a $(p + q - r)$ -dimensional solution. To determine a one-dimensional curve of singular points, we thus require $r = p + q - 1$ auxiliary equations to constrain the system. Following the above example, when the n -dimensional null vector at the critical state is introduced as the auxiliary variable \mathbf{v} , a singular curve in $p = 2$ parameters is appropriately constrained by the associated $r = n + 1$ auxiliary equations

$$\mathbf{K}_T \mathbf{v} = \mathbf{0}, \quad \text{and} \quad \|\mathbf{v}\|_2 = 1,$$

294 where the scalar equation restricts the magnitude of the eigenvector.

When evaluating one-dimensional curves ($r = p + q - 1$), one additional constraining equation is needed to uniquely solve the system of for a solution point

$$\mathbf{y} = (\mathbf{u}, \Lambda, \mathbf{v})$$

295 on the curve described by $\mathbf{G}(\mathbf{y})$. Hence,

$$\mathbf{G}^N(\mathbf{y}) \equiv \begin{pmatrix} \mathbf{F}(\mathbf{u}, \Lambda) \\ \mathbf{g}(\mathbf{u}, \Lambda, \mathbf{v}) \\ N(\mathbf{u}, \Lambda) \end{pmatrix} = \mathbf{0}, \quad (10)$$

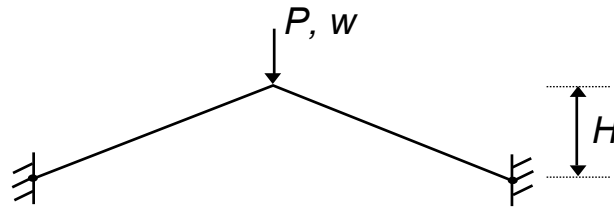


Figure 5. Schematic diagram of a toggle frame under transverse load P causing the frame to snap through with displacement w . The height H of the toggle frame is a free parameter that can be varied in a numerical continuation solver to investigate the system's snapping behaviour.

296 where N is a scalar equation that plays the role of a multi-dimensional arc-length constraint along a specific
 297 direction of the subset curve. Note that the system of equations for classical load-displacement equilibrium
 298 paths can be recovered by setting $p = 1$ and $q = r = 0$.

299 A solution to Eq. (10) can be obtained through a consistent linearisation coupled with Newton's method,

$$\mathbf{y}_k^{j+1} = \mathbf{y}_k^j - \left(\mathbf{G}_{,\mathbf{y}}^N(\mathbf{y}_k^j) \right)^{-1} \mathbf{G}^N(\mathbf{y}_k^j) \equiv \mathbf{y}_k^j + \delta \mathbf{y}_k^j, \quad (11)$$

300 where the superscript denotes the j^{th} equilibrium iteration and the subscript the k^{th} load increment. The
 301 iterative correction cycle is typically started by a predictive forward Euler step.

302 The above framework is quite general and can be adapted to find many different kinds of curves on an
 303 equilibrium surface; see Eriksson [17] or Groh et al. [18] for further details. The key is to define pertinent
 304 auxiliary equations that constrain the equilibrium equation to the locus of points required. Examples
 305 include:

- 306 1. Classic equilibrium paths in load-displacement space (a loading parameter is varied).
- 307 2. Parametric paths in parameter-displacement space (a geometric, constitutive or secondary loading
 308 parameter is varied).
- 309 3. Pinpointing singular points (bifurcation and limit points) on either of the two paths mentioned above.
- 310 4. Bifurcated branches emanating from a bifurcation point.
- 311 5. Singular paths that describe a locus of bifurcation and/or limit points in load-parameter-displacement
 312 space.
- 313 6. Branch-connecting paths that connect points on distinct equilibrium curves, *e.g.* a fundamental and a
 314 bifurcated path.

315 3.2 Illustrative example — snap-through of a toggle frame

316 As an example, consider the snap-through behaviour of the centrally loaded toggle frame with clamped
 317 ends, shown in Fig. 5. We start this idealised model with pre-defined geometry, material properties and
 318 loading to illustrate how the general algorithms can be used for a comprehensive investigation of structural
 319 stability and design parameter sensitivity. We shall evaluate the frame's fundamental load-displacement
 320 behaviour, including pinpointing all relevant singular points. Additional non-singular and singular curves
 321 are then traced by starting from a chosen solution on the fundamental path to explore the surrounding
 322 design space.

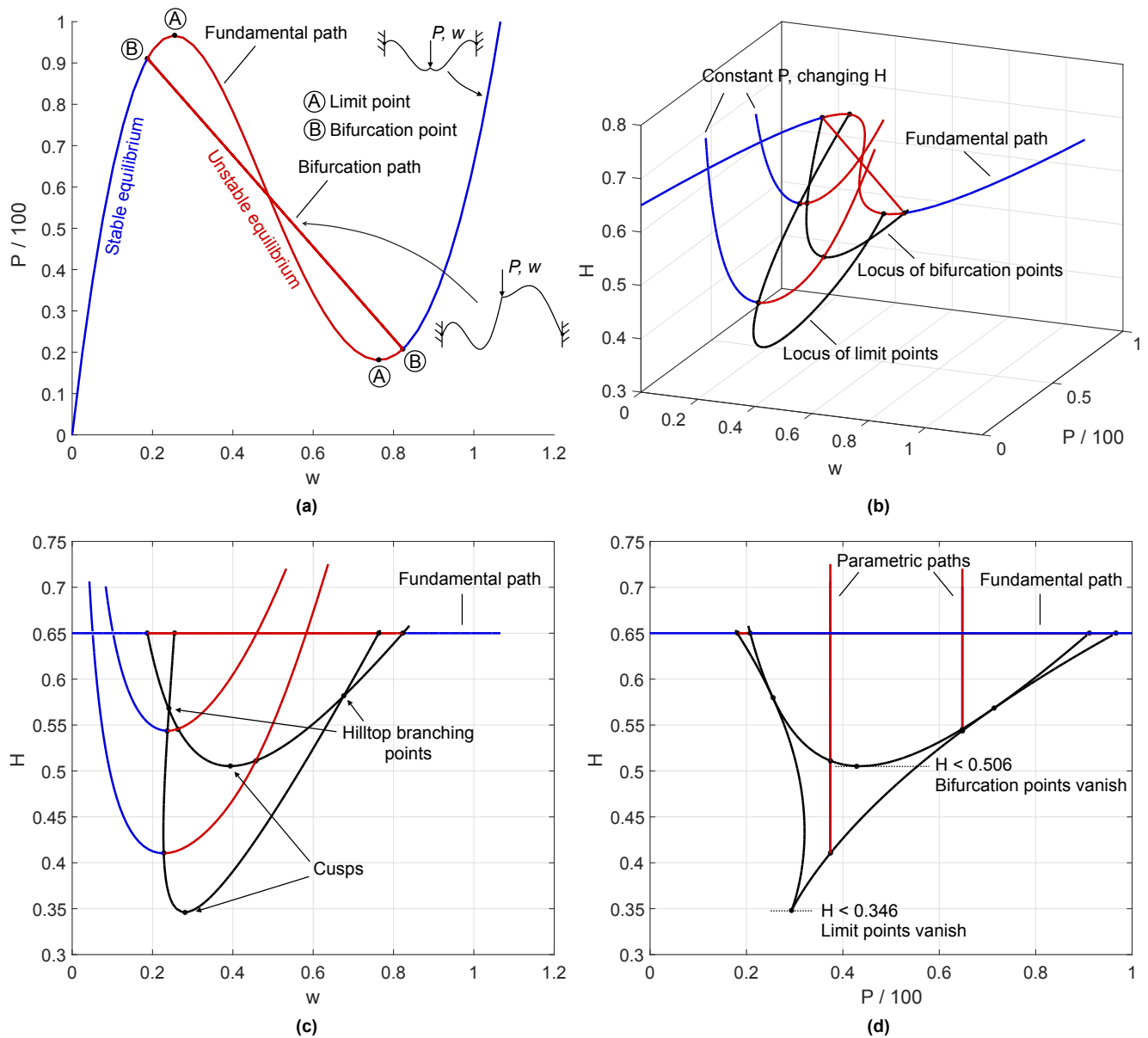


Figure 6. (a) Fundamental and bifurcation equilibrium paths of load (P) versus central displacement (w) for a toggle frame of height $H = 0.65$; (b) Isometric view of fundamental and bifurcation paths in displacement-load-height space, two additional parametric paths showing the relationship between height (H) and central displacement (w) at applied loads of $P = 37.4$ and $P = 64.8$, and locus of limit and bifurcation points with changing height; (c) and (d) Orthographic projections of (b) in displacement-height and load-height space respectively, indicating cusp catastrophes and hilltop-branching points.

323 The toggle frame initially deforms symmetrically on the fundamental equilibrium path. This deformation
 324 mode becomes unstable at a symmetry-breaking bifurcation just before the maximum limit point on the
 325 curve. Because the connected non-symmetric path branching from the bifurcation point is unstable, the
 326 toggle frame snaps dynamically into the inverted stable shape. In Fig. 6, blue segments denote stable
 327 equilibria, red segments denote unstable equilibria and black dots denote critical points.

328 Figure 6(a) restricts path-following to the classical displacement-load space. To illustrate generalised path-
 329 following capabilities, Fig. 6(b) extends the analysis to changes in the height H of the frame. Figure 6(b)

330 shows an isometric view in displacement-load-height space of the fundamental and bifurcation paths, plus
 331 two additional parametric paths. For these parametric paths, the applied load is held constant at $P = 37.4$
 332 and $P = 64.8$ respectively, and the relationship is traced between the height H and central displacement w .

333 By imposing a singularity condition in the generalised path-following algorithm, the locus of limit
 334 and bifurcation points can be traced, illustrating how changes in the height of the frame affect the load-
 335 displacement solution of these singular points. There are multiple benefits of tracing such fold lines. First,
 336 they can be used to identify interesting points such as the coincidence of limit and bifurcation points —
 337 the hilltop-branching points at $H = 0.567$ and $H = 0.581$ — or points where bifurcation and limit points
 338 cease to exist — the cusp catastrophes at $H = 0.506$ and $H = 0.346$. These points are clearly marked in
 339 the orthographic projections of Fig. 6(c) (w vs H) and Fig. 6(d) (P vs H). Second, fold lines can be used
 340 in design studies to determine the sensitivity of singular points with respect to design parameters, without
 341 having to perform computationally expensive Monte Carlo studies. Finally, fold lines can be used for
 342 optimisation purposes. For example, the displacement at the first instability can be maximised by reducing
 343 the height of the toggle frame to coincide with the hilltop-branching point at $H = 0.567$ (see Fig. 6(c)).

344 3.3 Application to the cylindrical shell

345 Consider a thin-walled isotropic cylindrical shell of thickness $t = 0.247$ mm, radius $R = 100$ mm and
 346 length $L = 160.9$ mm loaded in uniform axial compression via displacement control. The cylinder is
 347 linear elastic and isotropic with Young's modulus $E = 5.56$ GPa and Poisson's ratio $\nu = 0.3$, chosen to
 348 model Yamaki's longest cylinder (Batdorf parameter $Z = L^2\sqrt{1 - \nu^2}/Rt = 1000$) [31]. To represent a
 349 typical experimental setup as closely as possible, the cylinder is rigidly clamped at both ends with **axial**
 350 **compression/displacement u imposed at one end of the cylinder and the other end completely constrained.**

351 The cylinder is modelled using isoparametric, geometrically nonlinear finite elements based on a total
 352 Lagrangian formulation. The finite elements used are so-called "degenerated shell elements" [47] based
 353 on first-order shear deformation theory assumptions [48]. **The cylinder is discretised into 97 axial and**
 354 **241 circumferential nodes, that are assembled into 25-noded spectral finite elements using the element**
 355 **formulation of Payette & Reddy [49] and the large rotation parametrisation described by Bathe [50].** To
 356 reduce computational effort and complexity, only a quarter of the cylinder is modelled. **The circumferential**
 357 **domain is described by $s/R \in [-\pi, \pi]$ and the axial domain by $x/L \in [-0.5, 0.5]$ such that we model the**
 358 **quarter-segment $s/R \in [0, \pi]$ and $x/L \in [0, 0.5]$ with reflective symmetry conditions applied along the**
 359 **lines of symmetry.** In all figures that follow, blue segments denote stable equilibria, red segments unstable
 360 equilibria, and black dots critical points.

361 Figure 7(a) shows the equilibrium path starting from a single dimple, superimposed on the pre-buckling
 362 curve (fundamental path) in terms of normalised axial compression (uR/Lt) vs normalised load (P/P_{cl}).
 363 The classical buckling load is given by $P_{cl} = 2\pi Et^2/\sqrt{3(1 - \nu^2)}$. The stable pre-buckling curve runs
 364 diagonally in blue with the unstable single dimple solution running almost coincidentally alongside it.
 365 The unstable equilibrium branch of the latter starts at a limit point close to the first critical point on the
 366 pre-buckling path. This limit point is denoted by 0 in Fig. 7(a) with the corresponding normalised radial
 367 (out-of-plane) displacement (w/t) shown in Fig. 7(b). The deformation mode clearly shows a localised
 368 dimple in the centre of the domain.

369 Path-following in the direction of decreasing displacement leads to a *snaking* sequence. The reason
 370 behind snaking has been established in a number of related contexts as the behaviour of homoclinic orbits
 371 in the unfolding of a *heteroclinic connection* between flat and periodic states, see Hunt et al. [21] and
 372 references therein for an application to structural mechanics. The phenomenon is closely related to the

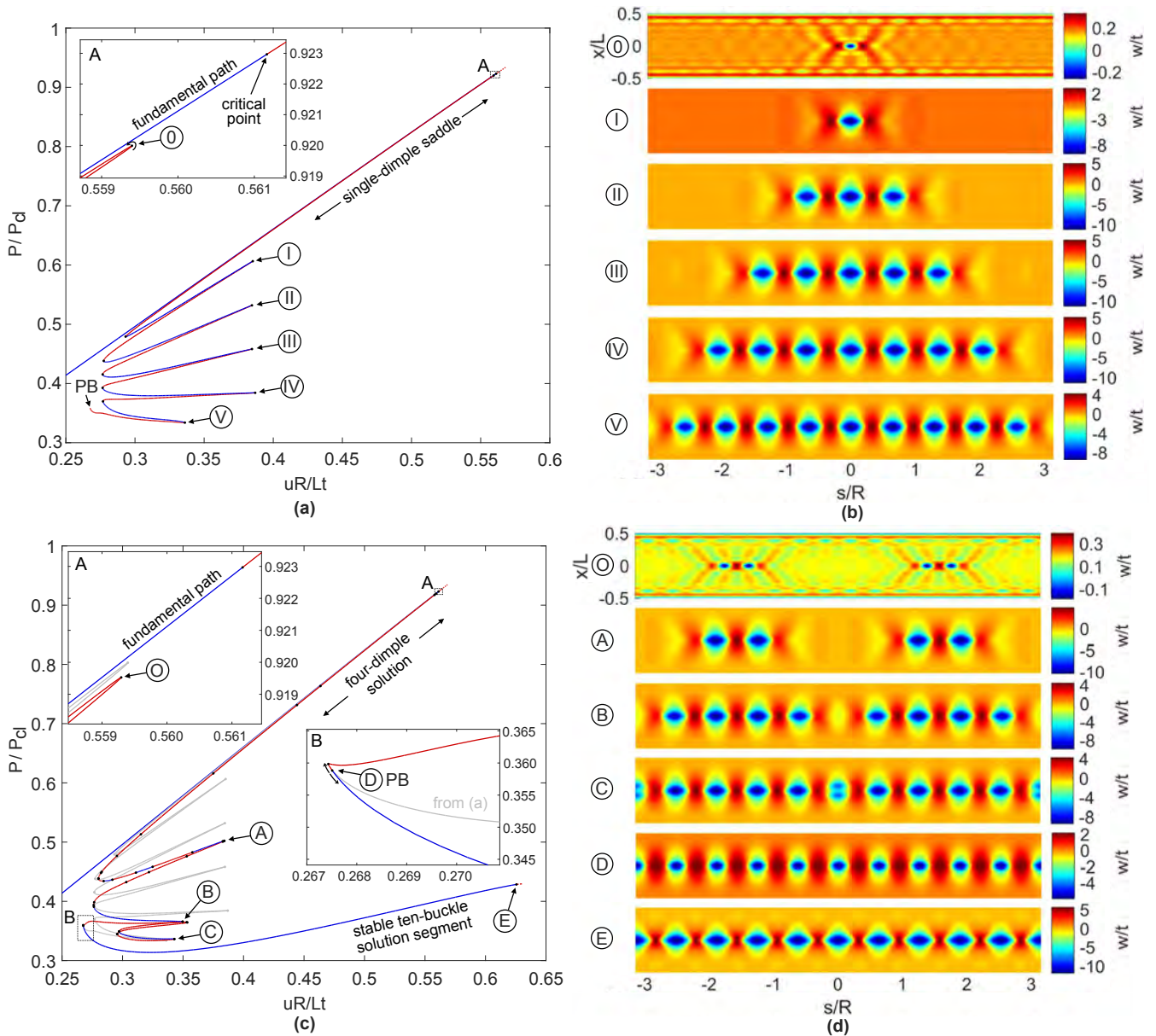


Figure 7. (a) Equilibrium path of a single-dimple post-buckling solution growing sequentially around the cylinder circumference through a series of destabilisations and restabilisations known as cellular buckling (or snaking). (b) Deformation mode shapes of the displacement component normal to the cylinder wall (w) over the cylinder domain (x is the axial coordinate and s the circumferential coordinate) for different points 0–V in (a). (c) Equilibrium path of a four-dimple post-buckling solution growing sequentially through cellular buckling. The single-dimple snaking solution in (a) connects to this path at a pitchfork bifurcation (see point D in inset B). (d) Radial deformation mode shapes over the cylinder domain for different points O–E in (c).

373 notion of front pinning around a Maxwell point, first described by Pomeau [51] in the context of fluid
 374 dynamics. For a recent review of snaking see Knobloch [52].

375 Starting from limit point 0 in Fig. 7(a), the single dimple becomes more pronounced with decreasing end-
 376 shortening and stabilises at a limit point ($uR/Lt = 0.293$, $P/P_{c1} = 0.479$). This critical point corresponds
 377 to the smallest possible compression to allow a single dimple as an equilibrium solution. Tracing the
 378 equilibrium path further, a series of destabilisations and restabilisations add further buckles to the left and

379 right of the original single dimple. Proceeding along the snaking path, the single dimple thus grows in
 380 a sequence of 1, 3, 5, 7, and 9 waves until an entire ring around the cylinder exists. The mode shapes
 381 corresponding to limit points I–V in Fig. 7(a) are shown in Fig. 7(b) and depict the series of increasing
 382 odd-numbered buckles (1, 3, 5, 7 and 9) spreading around the cylinder circumference. **This snaking**
 383 **sequence of odd buckles connects to another equilibrium path that preserves an additional symmetry group**
 384 **at pitchfork bifurcation point PB. This additional path is described next.**

385 The equilibrium path in Fig. 7(c) is an additional snaking sequence starting from two sets of two dimples
 386 located to the left and right of the original dimple (see Fig. 7(d)). In Fig. 7(c) the snaking path of the single
 387 dimple (from Fig. 7(a)) is shown in grey for reference and the new equilibrium path starting with two
 388 sets of two dimples is shown in red/blue. The four-dimple snaking path also originates at a limit point
 389 (O) close to the first critical point of the pre-buckling path (see inset A of Fig. 7(c)). With decreasing
 390 end-shortening, the snaking sequence grows from 4 to 8, and finally to 10 buckles. The mode shapes
 391 corresponding to various points on the red/blue path of Fig. 7(c) are shown in Fig. 7(d). The two equilibrium
 392 paths (grey and red/blue) are seen to connect at a pitchfork bifurcation (point D in inset B of Fig. 7(c)). In
 393 the immediate vicinity of this connection, the four-dimple snaking path regains stability at a limit point.
 394 The ten-buckle waveform is stable from $uR/Lt = 0.268$ until it destabilises at a pitchfork bifurcation
 395 (point E) at $uR/Lt = 0.626$. Beyond this bifurcation, an additional snaking sequence occurs, leading to
 396 the full Yoshimura post-buckling pattern. Additional rings of buckles all initiate from a single localisation
 397 and then spread circumferentially (see Groh and Pirrera [53] for more details).

398 **An additional snaking sequence starting from two dimples and representing growth of an even number**
 399 **of waves (2, 4, 6, 8 and 10) also exists. The even snaking sequence mirrors the behaviour of the odd**
 400 **snaking sequence in its pattern formation and in the connection to another equilibrium path at a pitchfork**
 401 **bifurcation. In systems featuring spatial localisation, snaking of both even and odd number of localisations**
 402 **is typical [52] and these solutions are often intertwined. This behaviour is also confirmed for the axially**
 403 **compressed cylinder and is shown in Fig. 8.**

404 Figure 8(a) shows the equilibrium path of the even snaking sequence in red/blue superimposed on the
 405 snaking solution of odd buckles in grey (from Fig. 7(a)). The even snaking sequence is also broken away
 406 from the pre-buckling equilibrium path and starts with the formation of two adjacent inward buckles (see
 407 point \emptyset Fig. 8(b)). These two buckles then multiply throughout the snaking sequence, with the equilibrium
 408 paths of the even and odd snaking sequences intertwined. The different mode shapes corresponding to limit
 409 points i–v in Fig. 8(a) are plotted in Fig. 8(b) and show the series of increasing even buckles (2, 4, 6, 8 and
 410 10) growing around the cylinder circumference.

411 The snaking solution of even buckles also ends at a pitchfork bifurcation (point PB in Fig. 8(a)) where
 412 it connects to another segment of the equilibrium path. This connecting equilibrium path is shown in
 413 Fig. 8(c) with the even-buckle path from Fig. 8(a) superimposed in grey. The two segments (red/blue and
 414 grey) of the equilibrium path connect at a pitchfork bifurcation (point d in inset B of Fig. 8(c)). The mode
 415 shape of point d in Fig. 8(d) confirms the expected ten-buckle waveform. In conclusion, both the odd- and
 416 even-buckle curves lead to an axially localised post-buckling state of a single ring of ten diamonds.

417 In closing this section we remark that the snaking results for the present paper were obtained with a mesh
 418 $4\times$ denser than those in Ref. [53]. While the overall behaviour of the snaking sequence and the nature of
 419 pattern formation is unchanged, the refined results presented here update and eliminate the second-order
 420 snaking features originally observed in Ref. [53].

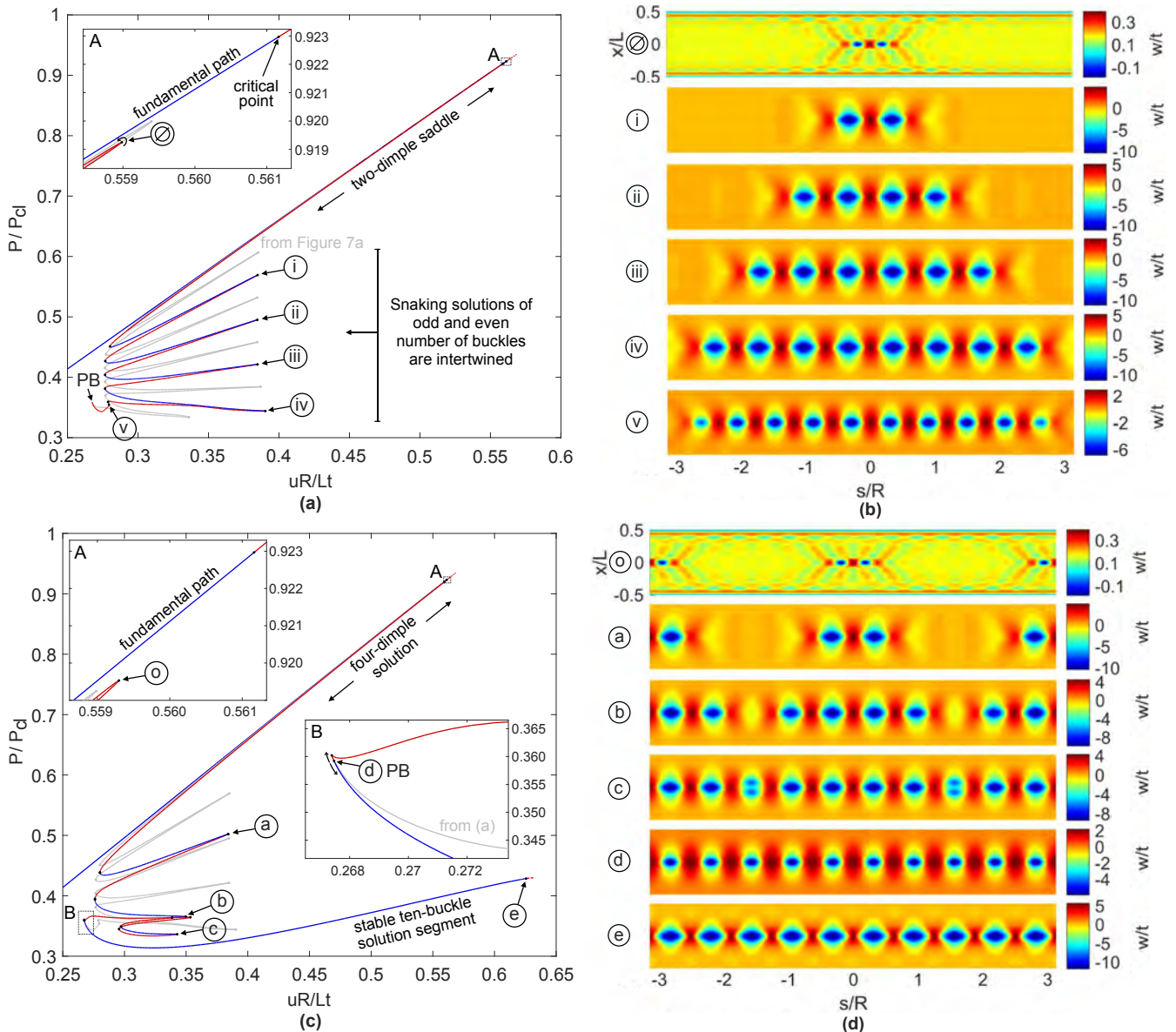


Figure 8. (a) Equilibrium path of a double-dimple post-buckling solution growing sequentially around the cylinder circumference through a series of destabilisations and restabilisations known as cellular buckling (or snaking). (b) Radial deformation mode shapes over the cylinder domain for different points \emptyset –v in (a). (c) Equilibrium path of a four-dimple post-buckling solution growing sequentially through cellular buckling. The single dimple snaking solution in (a) connects to this path at a pitchfork bifurcation (see point d in inset B). (d) Radial deformation mode shapes over the cylinder domain, for different points \emptyset –e in (c).

4 ENERGY BASED METHODS — MAXWELL AND MOUNTAIN-PASS CRITERIA

421 While continuation methods are an integral part of unraveling the often complex behaviour associated with
 422 subcritical instabilities, they do not tell us which state (energetically) the system would prefer, nor quantify
 423 the sensitivity of a locally metastable equilibrium state, so-called *shock sensitivity*. We can therefore
 424 supplement our continuation approach with energy-based methods to explore these questions more directly.

425 4.1 Maxwell load versus Maxwell displacement

426 To address the problem of an infinite pre-buckling critical load (as in Fig. 3(b)), one option is the
 427 Maxwell equal-energy criterion. This criterion originates from the concept of the Gibbs free energy in
 428 thermodynamics, to address state transitions triggered by statistical fluctuations or disturbances [54, p. 53].
 429 Here, stability is governed only by the global minimum of total potential energy. Under some form
 430 of parametric variation such as load or applied displacement, the Maxwell criterion provides the first
 431 circumstance for which the energy of a post-buckled state first falls below the energy minimum of the
 432 pre-buckled state. The reasoning is that, upon increase of the parameter, this would be the first time the
 433 system could be shaken out of its trivial state and transition to the post-buckled global minimum. Although
 434 the Maxwell criterion cannot be considered a hard and formal point of instability, it may, nevertheless,
 435 serve as a useful and robust lower-bound estimate for instability in systems where small disturbances and
 436 imperfections have pronounced effects.

437 A long structural system loaded axially typically prefers a localised to a distributed post-buckled response
 438 [32]. If the localised buckle subsequently restabilises, additional cells of buckling will often develop in
 439 adjacent positions to the first via a sequence of localised instabilities, according to the snaking mechanism
 440 described for the cylinder above. Typically, the load tends to fluctuate or *snake* between upper and lower
 441 limits as the sequence progresses. The *Maxwell load*, defined (as above) as the lowest load for which the
 442 post-buckled energy matches its pre-buckled counterpart, lies between the two limits, and effectively acts
 443 as an organizing centre about which the post-buckled load oscillates as the snaking progresses.

444 This snaking sequence with localisations developing over the length of a structure has now been
 445 recognised in a number of different circumstances (see for example [55, 56, 57, 58, 59]). However,
 446 in Section 3.3 we describe an alternative snaking scenario, in which localised buckles trigger not axially
 447 but orthogonal to the direction of the applied load, around the circumference of a buckling cylindrical shell.
 448 In this sequence, a *Maxwell displacement* rather than a Maxwell load acts as the organizing centre, with the
 449 system fluctuating between two limits of end-shortening as the load continues to fall. Two examples of
 450 such snaking behaviour are seen in Figs. 7(a) and (c).

451 4.2 Mountain pass algorithms

452 First introduced by Ambrosetti and Rabinowitz [60], the Mountain Pass Lemma is a fundamental
 453 mathematical tool for proving the existence of stationary points of nonlinear functionals. Excluding some
 454 technical details, the key ingredients of the theorem are:

- 455 1. a suitable (energy) functional $\mathcal{W}(x)$
- 456 2. a stationary point e_1 , which is a local minimum
- 457 3. a second point e_2 , for which $\mathcal{W}(e_1) > \mathcal{W}(e_2)$

458 **We note that a suitable function is normally available in the form of total potential energy, with local**
 459 **minima appearing on a stable fundamental equilibrium path [7].**

The theorem states that, over the set of all continuous paths connecting e_1 and e_2 , *i.e.*:

$$\Gamma := \{\gamma \in C[0, 1] : \gamma(0) = e_1 \quad \text{and} \quad \gamma(1) = e_2\},$$

one can find the infimum of the maxima of the energy functional $\mathcal{W}(u)$ along any path $\gamma \in \Gamma$. This infimum is the mountain pass solution and is a saddle point

$$\mathbf{x}_c := \inf_{\gamma \in \Gamma} \left[\max_{\mathbf{x} \in \gamma} \mathcal{W}(\mathbf{x}) \right].$$

The physical significance of the mountain pass is that it represents the connecting point in solution space with the smallest energy hump,

$$\Delta \mathcal{W}_c = \mathcal{W}(\mathbf{x}_c) - \mathcal{W}(\mathbf{e}_1),$$

460 required to escape the local minimum at \mathbf{e}_1 and transition to a lower energy state at \mathbf{e}_2 . Therefore the
 461 Maxwell load/displacement (depending on the loading regime), at which $\mathcal{W}(\mathbf{e}_1) = \mathcal{W}(\mathbf{e}_2)$, marks the
 462 onset of the ability to jump to such a lower energy state, and therefore the onset of ‘‘shock sensitivity’’ in
 463 the system.

464 The application of the Theorem provides a computable energy hump to assess shock sensitivity; the
 465 mountain pass state \mathbf{x}_c itself is significant, since at this point the system has just one negative eigenvalue
 466 for which the system is unstable. This eigenvector marks a direction in solution space \mathbf{m} tangent to the
 467 mountain path γ , and suggests a mode shape that if applied to the system would most easily induce
 468 transition from \mathbf{e}_1 to \mathbf{e}_2 . This eigenvalue at the mountain pass point therefore indicates the imperfection or
 469 probing modes that a subcritical system could be most sensitive to.

470 The literature gives a variety of algorithms for finding mountain pass solutions *e.g.* the nudged elastic
 471 band method [61], the dimer method [62] and conjugate peak refinement [63]. Here we briefly describe the
 472 latter, as it is used later to illustrate shock sensitivity of the axially-compressed cylinder.

473 Conjugate peak refinement is an iterative scheme performing alternating line search maximisation
 474 and minimisation steps to find the mountain pass solution \mathbf{x}_c . The approach generates a sequence of
 475 piecewise-linear approximations to a path γ^* which passes through \mathbf{x}_c . For the k^{th} iteration, we denote this
 476 approximation $\gamma^{(k)}$ characterised by a set of points $\Gamma^{(k)} := \left\{ \mathbf{x}_i^{(k)} \right\}_{i=1}^{k+1}$. We start the process by defining
 477 $\gamma^{(0)}$ as the straight line connecting \mathbf{e}_1 and \mathbf{e}_2 , so that $\Gamma^{(0)} = \{\mathbf{e}_1, \mathbf{e}_2\}$. Then starting with $k = 1$, each
 478 iteration comprises three steps:

479 **Line Search Maximisation.** We maximise the functional $\mathcal{W}(\mathbf{x})$ along the piecewise linear path $\gamma^{(k-1)}$,
 480 to obtain line maximisation point $\hat{\mathbf{x}}^{(k)}$ lying between points $\mathbf{x}_j^{(k-1)}$ and $\mathbf{x}_{j+1}^{(k-1)}$.

481 **Line Search Minimisation.** We then find the scalar α such that $\mathcal{W}(\hat{\mathbf{x}}^{(k)} + \alpha \mathbf{s})$ attains a minimum, where
 482 the search direction \mathbf{s} is chosen to be

$$\mathbf{s} = -\mathbf{g} + \frac{\mathbf{g}^T \mathbf{h}}{\mathbf{d}^T \mathbf{h}} \mathbf{d}^T \quad \text{where} \quad \mathbf{d} = \nabla \left(\gamma^{(k)} \right) \quad \text{and} \quad \mathbf{g} = \nabla \mathcal{W}(\hat{\mathbf{x}}^{(k)}) \quad (12)$$

Update mountain path $\gamma^{(k)}$. We then add the new point $\hat{\mathbf{x}}^{(k)} + \alpha \mathbf{s}$ to the path to form $\gamma^{(k)}$, so that points
 defining the line are

$$\Gamma^{(k)} := \left\{ \mathbf{x}_0^{(k-1)}, \dots, \mathbf{x}_j^{(k-1)}, \hat{\mathbf{x}}^{(k)} + \alpha \mathbf{s}, \mathbf{x}_{j+1}^{(k-1)}, \dots, \mathbf{x}_k^{(k-1)} \right\}_{i=1}^{k+1}.$$

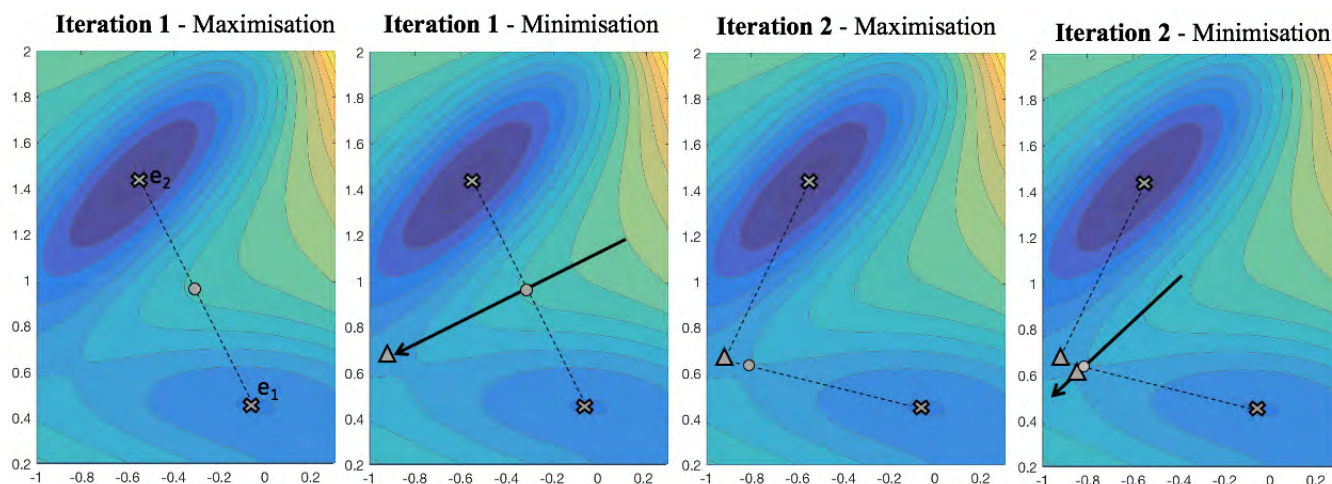


Figure 9. Symbols denote: (×) Local minima, (— — —) potential ‘mountain path’, (—→) search direction ○ line maximum, Δ line minimum.

483 At any iteration of the state $\hat{\mathbf{x}}^{(k)} + \alpha \mathbf{s}$ is the best approximation of the mountain pass solution. The rate of
 484 convergence can be determined by computing the gradient at this point, to ensure it is stationary, as well as
 485 determining the lowest two eigenvalues of the energy’s Hessian, since only the smallest must be negative.

We now demonstrate the mountain pass procedure geometrically with a generic, two degree-of-freedom energy landscape given by a modified Müller-Brown potential [64]. This particular potential (Fig. 9) has application in computational chemistry [63]. It is chosen since it has no symmetry, and is characterised by two local minima at e_1 and e_2 , with a non-trivial mountain pass connecting them. The approach provides a good approximation to the saddle point in just two iterations. In the first iteration, we see the algorithm starts by approximating the mountain path with a straight line between the e_1 and e_2 . A maximum is located along this line; see the ○ in the far left panel of Fig. 9. A minimum in the conjugate direction (12) is then found, as indicated by the symbol Δ in the next left-most panel. Thus, the first iteration provides a reasonable approximation to the saddle. The path $\gamma^{(0)}$ is updated to $\gamma^{(1)}$, characterised by three points connected by the pair of straight lines. For iteration 2 the procedure continues in the same way, first a maximisation step over the path to produce the second ○ in the third panel of Fig. 9, followed by a minimisation problem in the conjugate direction to the path through the maximum point. For this example, the newly found minimum on this path (the second Δ in the right-most panel of the figure) satisfies the tolerance condition

$$\|\nabla \mathcal{W}(\mathbf{x}_c)\|_e < \epsilon = 1 \times 10^{-5},$$

486 and the algorithm terminates.

487 4.3 Application to the cylindrical shell

488 Classically, stability of equilibrium is governed entirely by the local Hessian of the total potential energy;
 489 wells with respect to all degrees-of-freedom denote stability, whereas saddles or maxima denotes instability.
 490 This framework fails in the case of infinite critical loads presented in Figure 3, where two equilibrium
 491 paths are separated by a small energy barrier but never strictly intersect. Thus, although the idealised
 492 **structure never transitions out of the trivial equilibrium state**, that state becomes metastable, where small
 493 disturbances could trigger instability.

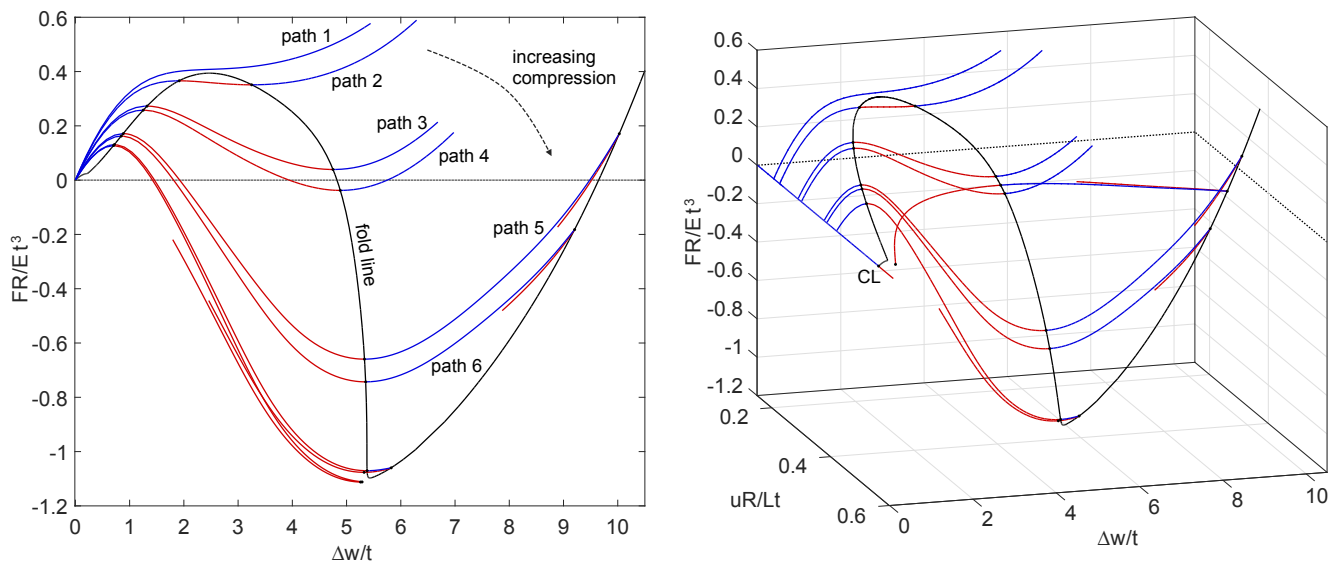


Figure 10. The stability landscape of an axially compressed cylinder with a probing side force. (a) Normalised probe force (FR/Et^3) vs normalised probe displacement ($\Delta w/t$) for different values of normalised axial compression (uR/Lt). (b) The stability landscape in terms of axial compression vs probe force vs probe displacement.

494 As is seen in the insert of Figure 7(a), the cylinder too features an equilibrium path that asymptotically
 495 converges to, but never actually intersects, the pre-buckled path. Here, we compare the energy levels of the
 496 pre-buckling path and the circumferentially periodic equilibrium path of a single ring of diamonds (path
 497 ending in point E in Figure 7(d)). As load is applied in a rigid manner (controlled end-shortening), the
 498 stability threshold corresponds to a Maxwell *displacement* and this computes to be $M_u = u_M/u_{cl} = 0.486$
 499 ($u_M R/Lt = 0.294$). It is interesting to note that this value correlates well with the limit point ($uR/Lt =$
 500 0.294) in Figure 7(a).

501 The Maxwell displacement could serve as a lower-bound estimate for the cylinder’s first instability load,
 502 by marking the onset of “shock sensitivity” [65] — *i.e.* that of metastability of the pre-buckling path.
 503 This snaking sequence marking the development of a single dimple into a buckle pattern that is periodic
 504 circumferentially but localised axially, is in marked contrast to the snaking at the lower Maxwell load of
 505 such rings developing to a fully periodic pattern identified in earlier work [66, 40].

506 Rather than apply a computationally expensive infinite degree-of-freedom mountain-pass algorithm as in
 507 Horák et al. [35], another way of looking for the mountain-pass solution is to test the cylinder’s resilience
 508 to the single-dimple localisation; how much displacement is necessary to trigger a dynamic escape from
 509 stable pre-buckling to a post-buckled state via the mountain-pass saddle? We could envisage perturbing the
 510 cylinder from the side using a hypothetical infinitesimally-thin, infinitely-stiff, probe or poker; experimental
 511 implementation of this idea is explored in Section 5 below.

512 To implement such an analysis numerically, consider applying such a poker at right angles to the cylinder
 513 mid-surface, half-way along its length. Such a process involves two fundamental parameters, applied
 514 end-compression u and lateral probing force F . We consider applying such a probe repeatedly as the
 515 axial compression is quasi-statically increased. The results are presented in Fig. 10. At low levels of axial
 516 compression, we find a nonlinear softening/stiffening relationship of strictly positive stiffness between the
 517 probe force F and the ensuing dimple displacement Δw ; see path 1 in Figure 10(a). Here Δw denotes
 518 radial displacement relative to the radial (Poisson) dilation that naturally occurs in the pre-buckling state.

519 For increased levels of end-shortening, the equilibrium manifold traces S-shaped curves; as the dimple
 520 develops, lateral resistance reduces, until limit points are traversed leading to regions of negative stiffness
 521 (paths 2–3 in Fig. 10(a)). For even greater end-shortening, the probe force reduces significantly, dipping
 522 below the zero load axis (*e.g.* $F = 0$ on path 4). At this point an unstable saddle state is encountered,
 523 corresponding to the single-dimple mountain-pass solution. Also shown in Figure 10(a) is a black fold
 524 line connecting maximum and minimum limit points, and thereby describing a boundary that separates the
 525 domain into stable and unstable regions.

526 Figure 10(b) expands this landscape into three dimensions, providing an interesting stability landscape
 527 that qualitatively matches the experimental results of Viro *et al.* [67] on a different cylinder. The area
 528 between the stable pre-buckled and unstable single-dimple solutions under the F vs Δw curve represents
 529 the energy barrier, and thereby the “shock sensitivity” of the pre-buckling state. The size of this energy
 530 barrier can be understood qualitatively by plotting the fold line connecting maximum and minimum points;
 531 see Figure 10(b). This curve slopes down towards the buckling point on the pre-buckling path (point CL).
 532 Indeed, the fold line intersects the buckling point on the pre-buckling path, confirming that resilience of the
 533 pre-buckling state to small perturbations (*i.e.* the linear stability) indeed vanishes at that point.

5 EXPERIMENTAL METHODS FOR EXPLORING INSTABILITIES

534 While numerical methods for the analysis of nonlinear structures are well-developed, experimental methods
 535 tailored to such structures, in particular shell buckling, have received comparatively little attention; see
 536 *e.g.* [68, 69, 70, 31, 71, 20, 67, 72]. The trend in modern engineering is to test experimentally for single
 537 parameter values, and then use computational models, virtual testing, and “digital twins” wherever possible
 538 to extend the envelope. However, for fundamentally imperfection-sensitive buckling problems, such an
 539 approach will not explore the stability landscape reliably. Hence there is a fundamental barrier to researchers
 540 hoping to exploit nonlinear structures concepts for industrial applications. This barrier has arguably led to
 541 over-conservative designs in safety-critical industries like the aerospace sector, which requires stringent
 542 testing before new components are allowed to fly. Organisations such as NASA have therefore put renewed
 543 emphasis on experimental testing, and in particular, feeding high-fidelity imperfection measurements of
 544 specimens into models [72].

545 5.1 Experimental path-following

546 Conventional test methods fail to capture all but the simplest nonlinear behaviour, and consequently
 547 researchers lack reliable methods to validate their ideas experimentally. The main reason traditional test
 548 methods fail is the difficulty in measuring unstable parts of the response. Any structure whose equilibrium
 549 curve features limit points can snap under force- or displacement-controlled test methods, as illustrated
 550 in Figure 11(a). Such snap-through thus gives rise to regions of the equilibrium curve that might seem
 551 inaccessible experimentally.

552 Numerical analysis succeeds where experiments fail because in a numerical setting the force and
 553 displacement at a control point can be controlled *independently* and *simultaneously*. This freedom allows
 554 the solver to set combined limits on force and displacement, and prevents jumping to other solutions
 555 when an equilibrium becomes unstable (see Figure 11(b) for an illustration of the arc-length method).
 556 Consequently, displacement limit points can be traversed, unstable paths followed, and the full nonlinear
 557 response of a structure described. In an experimental setting, the force and displacement of a control point
 558 are linked by the elasticity of the structure; meaning that one can control the displacement of a control

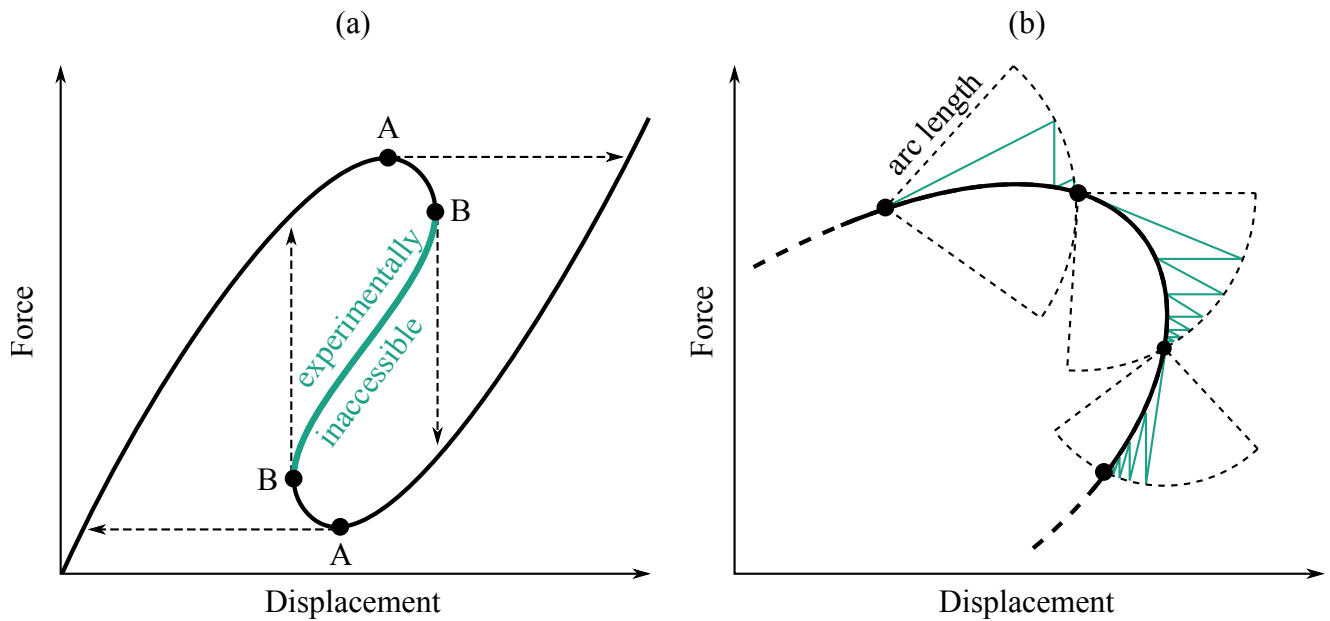


Figure 11. (a) Schematic of a nonlinear force-displacement curve featuring both displacement and force limit points. At a force limit point (A) force-controlled test methods snap across. At a displacement limit point (B) displacement-controlled methods snap down. (b) Schematic of an arc length-based numerical solution traversing a displacement limit point. The green line represents the iterative solutions of a Newton-Raphson based method.

559 point and generate a reaction force, or *vice versa*, but not both. This coupling makes it impossible to apply
 560 numerical techniques to experiments without some additional control.

561 There are several interesting published approaches to work around this problem. Wiebe and Virgin [73]
 562 use a hammer to trigger snap-through of a shallow arch. By analysing the transient dynamic trajectories of
 563 the structure during the snap, locations of unstable static equilibria are deduced. By intentionally allowing
 564 snap-through, this method can locate unstable equilibria without needing to actively control them. Viro
 565 et al. [67] use a poker to laterally probe a cylinder under increasing axial load. By tracking changes in
 566 the probe force-displacement curves, they can estimate the load at which the cylinder becomes globally
 567 unstable, before the instability load is reached. The concept of probing is especially relevant to the work
 568 presented here: an experimental path-following method which utilises probes to stabilise and control
 569 unstable equilibria.

570 5.2 Application to a shallow arch

571 Consider the centrally-loaded shallow arch studied by Neville et al. [74] shown in Figure 12(a), with
 572 dimensions $L = 205$ mm, $h = 20$ mm, $t = 1.5$ mm, and depth = 5 mm. For symmetric deformations,
 573 the structure exhibits the complex nonlinear behaviour shown in Figure 12(c). Looking at the first few
 574 “petals” (starting at one of the two fundamental equilibria and following the equilibrium path towards the
 575 other), it is clear that the response comprises many successive displacement limit points. A displacement-
 576 controlled experiment would only obtain the first two segments of the equilibrium curve (the solid lines in
 577 Figure 12(d)), snapping from one to the other at limit points L_1 and L_2 .

578 At $u_a = 5$ there are several equilibria available; each with distinct values of F_a . Each equilibrium is
 579 also associated with a unique deformation shape (Figure 12(e)), where the unstable equilibria correspond
 580 to more complex shapes. Controlling the structural shape allows us to stabilise unstable equilibria, and

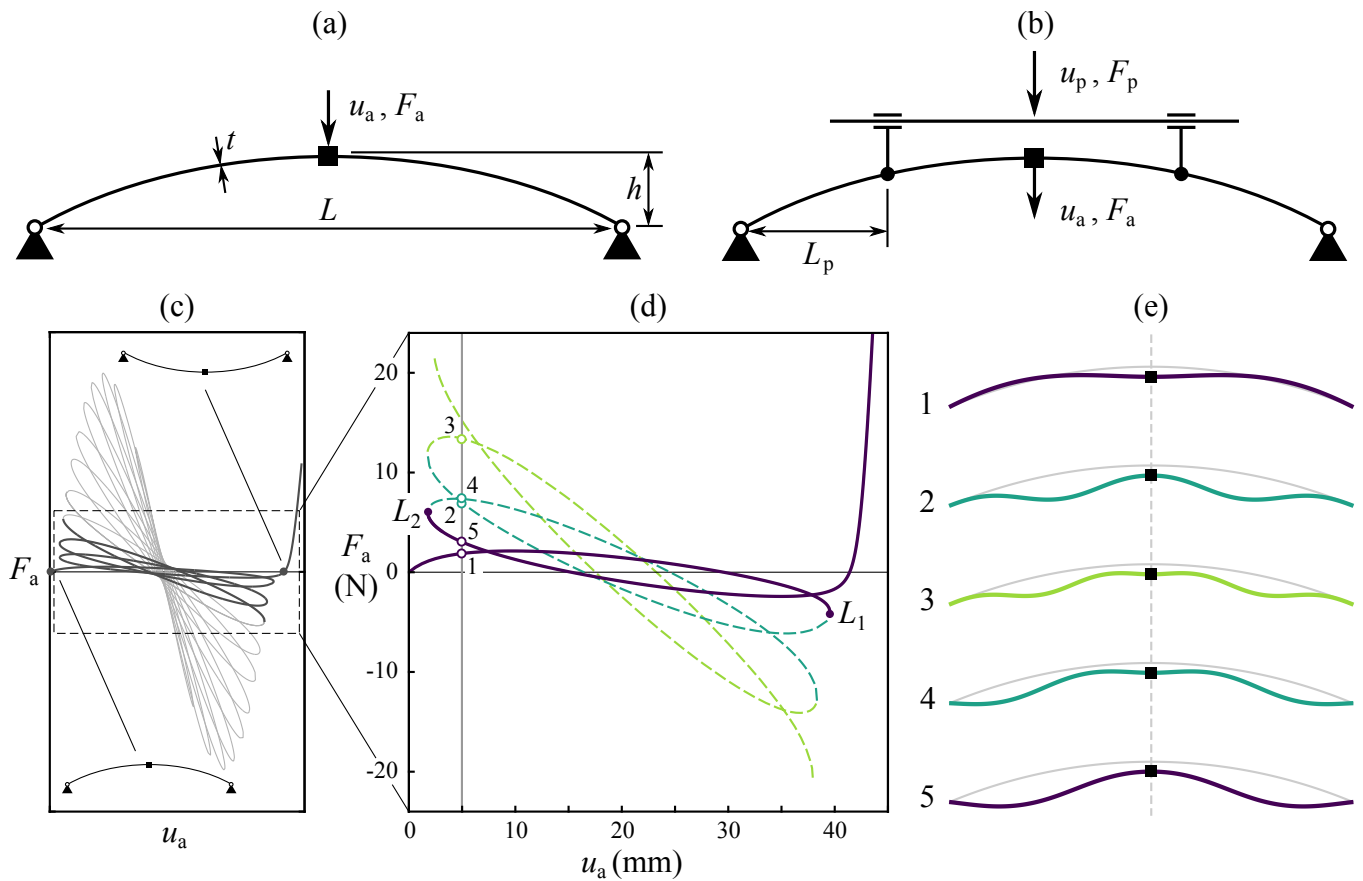


Figure 12. (a) Geometry of the shallow arch. The depth of the arch is not labelled; this dimension is measured into the page. Displacement u_a is applied at the mid-span actuation point, generating reaction force F_a . (b) Modified geometry including two “probes”. Symmetry is maintained by enforcing vertical displacement u_p across both probes, while they are allowed to move horizontally. (c) FEA prediction of the full equilibrium curve from one fundamental state to the other. (d) A subset of the equilibrium curve, starting from each of the fundamental equilibria and showing only the first two limit points on each side; equilibria available at $u_a = 5$ mm are numbered 1–5. (e) Deformation shapes associated with equilibria 1–5. This figure has been redrawn from the figures in [74].

581 indirectly influence the reaction force on a displacement-controlled control point. Having decoupled the
 582 force and displacement experimentally, numerical approaches become viable. Two extra probes provide
 583 control over the deformation shape as shown in Figure 12(b). Such probes produce reaction forces that
 584 change the structure. However, when the probe reaction force equals zero, then it is an equilibrium of the
 585 unperturbed structure. Crucially, reaction force is also zero at unstable equilibria—in this case the probes
 586 provide the infinitesimal restoring force required to prevent the instability from growing. By applying a
 587 large probe perturbation at a stable equilibrium, the probes can be used to search for other equilibria.

588 By moving the probes and actuation point in concert, a simple form of path-following can be performed
 589 [75]. The actuation point steps forward, then the probes search for equilibrium ($F_p = 0$). Small perturbations
 590 can be used to avoid large deviations from the equilibrium curve. If the actuation point steps past a limit
 591 point, the probes will not be able to find equilibrium and the actuation point direction is then reversed.
 592 This approach allows the equilibrium path of the shallow arch to be followed around a displacement limit
 593 point, as shown in Figure 13(b). Deformation shapes of the arch at several points in the experiment are also
 594 shown in Figure 13(c). Shapes 1 and 2 are the two fundamental equilibria (also shown in Figure 12(c)).
 595 Shape 3 corresponds to stable equilibrium, and resembles shape 1 in Figure 12(e). Shape 4 corresponds

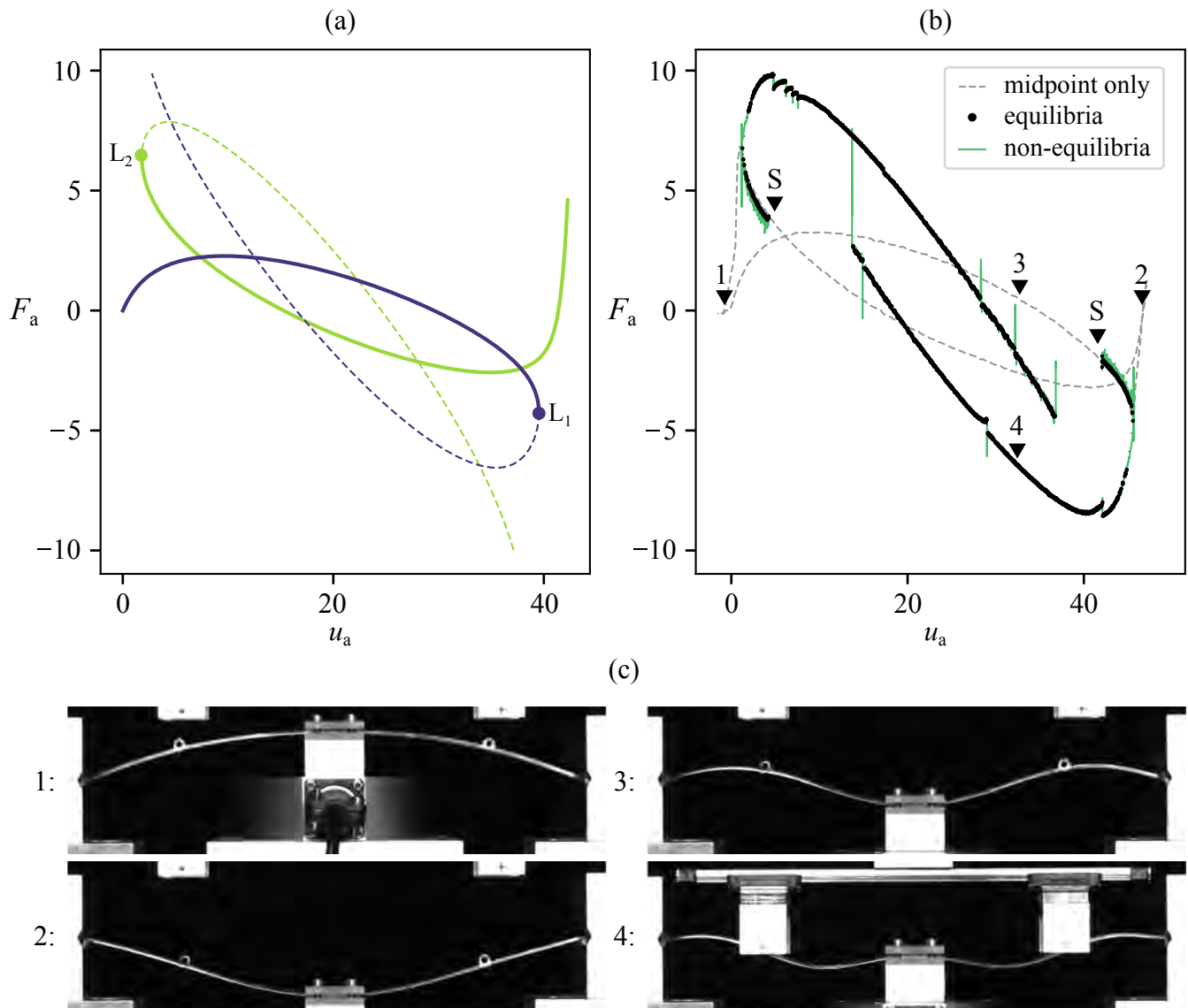


Figure 13. Results of the experimental path-following method. (a) FEA prediction of a subset of the equilibrium curve. Solid and dashed lines indicate stable and unstable segments, respectively. (b) Equilibrium curves obtained in a path-following experiment from [76]. The dashed grey line was obtained using displacement control on the midpoint only. The path-following algorithm was started at the two points marked “S”. Non-equilibria (e.g. $|F_p| > 0.1$ N when searching for equilibria) are shown in green, and equilibria ($F_p < 0.1$ N) are indicated by the black dots. (c) Deformation shapes of the arch during the experiment. Shapes 1–4 correspond to the markers 1–4 in (b).

596 to unstable equilibrium, and consequently is more complex. It resembles shape 2 in Figure 12(e), which
 597 corresponds to the same segment of the equilibrium curve.

598 Experimental results are naturally affected by phenomena and imperfections not included in theoretical
 599 models. The shallow arch example, for instance, is sensitive to changes in geometry and probe location,
 600 as well as displaying complex behaviour in response to the two input parameters (u_a and u_p). Virtual
 601 testing is a technique that can address these issues, and aid in experimental design and interpretation of
 602 results. A successful example of such a virtual testing environment coupled to the commercial FE solver
 603 ABAQUS is presented in [75]. A finite-element model is used to simulate a “perfect” experiment—*i.e.* one
 604 in which the equipment and test specimen behave exactly as intended. The model includes limitations of

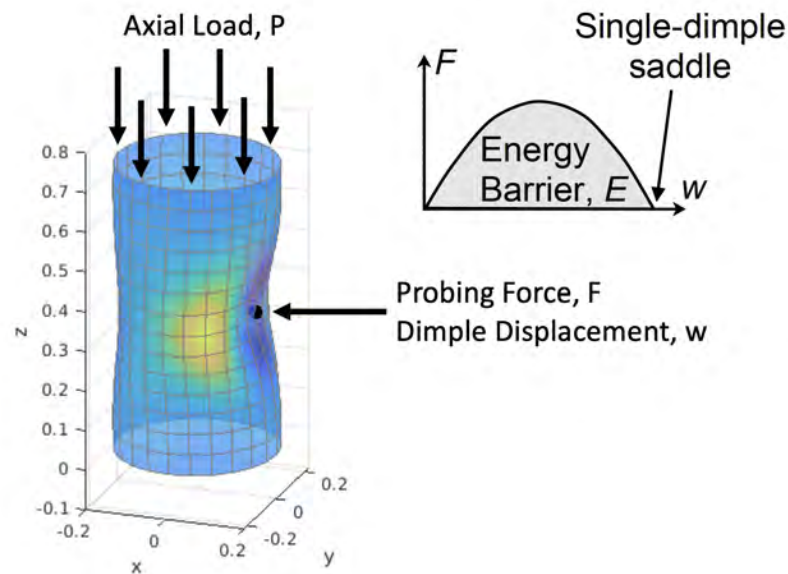


Figure 14. Test for assessing the resilience of the cylinder to perturbations, proposed by Thompson [65] and Thompson & Sieber [11].

605 the experimental setup—*e.g.* sensor noise, limited number of control points, *etc.*—and provides the same
 606 inputs and outputs that are available in the real experiment. This virtual testing environment provides a
 607 useful middle ground between numerical solutions and experiments, and serves as a “sandbox” or digital
 608 twin to explore the effects of different test configurations and imperfections.

609 5.3 Experimental mountain-pass methods — “a game of poker”

610 Inspired by the theoretical work of Horák *et al.* [35], Thompson *et al.* [65, 11] observed that the mountain-
 611 pass state for an axially-compressed cylinder looks remarkably similar to the small dimple induced by
 612 probing the cylinder laterally with a finger. The authors discuss a thought experiment where the cylinder’s
 613 resilience to perturbations (*i.e.* linear stability) is tested by probing the cylinder radially inwards using
 614 a poker (see Fig. 14). In fact, the idea of poking axially-compressed cylinders from the side to assess
 615 resilience to buckling has a long history predating any mountain-pass considerations. By tapping axially-
 616 loaded cylinders with a finger Eßlinger and Geier [77] found stabilised single-dimple states. Hühne *et*
 617 *al.* [71] realised that the single dimple can act as an imperfection, that excites the characteristic observed
 618 buckling behaviour. They set out to out to determine a robust lower bound to buckling load that could
 619 replace the empirically determined knockdown factors proposed in NASA’s SP-8007 [78] guideline. Over
 620 the last decade, this methodology has led to a battery of tests on composite cylinders [79], and extensions
 621 to probabilistic perturbation [80] and multiple perturbation loads [81].

622 The poker force *vs* displacement response of the cylinder for different levels of axial compression
 623 was shown previously using FE simulations in Fig. 10(a). Once these S-shaped curves pass through the
 624 zero-poker-force axis, the single dimple exists as an unstable saddle solution and a dynamic escape via the
 625 mountain pass is possible. The likelihood of such an escape can be quantified by the mountain-pass energy
 626 barrier, represented by the area enclosed by the associated force/displacement curve and force axis. In
 627 Fig. 10(a) it is readily observed that the greater the applied axial compression, the smaller the energy barrier
 628 provided by the single-dimple mountain pass. Thus, by repeating the poking procedure for multiple levels

629 of axial compression and computing the energy barrier up to the mountain-pass point, a non-destructive
 630 testing method can be established that provides a *safety cushion* before buckling is likely to occur.

631 Such a probing experiment was successfully implemented by Viro *et al.* [67]. By controlling the
 632 displacement of the lateral poker, the unstable mountain-pass point was determined when the reaction force
 633 on the poker vanished; this state replicating that of an unprobed cylinder. Furthermore, by aggregating
 634 the poker force *vs* poker displacement curves for multiple levels of compression, a stability landscape
 635 emerged that qualitatively matched Fig. 10(b). An experimental buckling load of the cylinder could also
 636 be determined by recording the level of compression for which it lost its ability to resist the poking
 637 displacement, *i.e.* the reaction force fell beneath a specific tolerance.

638 Even though the idea is simple to implement, in practice the system can bifurcate by pivoting around
 639 the point load. To offset this symmetry-breaking effect, as highlighted by Thompson and Sieber [11],
 640 a second control probe is often required. Second, the choice of probing location needs to be carefully
 641 chosen, as different locations can lead to differing buckling load predictions [82]. Finally, there are practical
 642 shortcomings to obtaining the mountain-pass state for arbitrary systems. For the cylinder, the mountain-pass
 643 state happens to be a relatively simple single-dimple localisation, but in general, it could be more intricate,
 644 and may be difficult to impose by one or even multiple pokers. Combining poking experiments with
 645 experimental path-following algorithms may well prove a fruitful avenue for future research.

6 EXPLOITING BUCKLING INSTABILITIES

646 As stated in the Introduction and indeed reflected in the title of this paper, instability need not solely be
 647 considered as something to be avoided or designed against; it is also possible to utilise instability in a
 648 positive manner [3]. We highlight three areas where such benefits can be found in different engineering
 649 domains and length-scales.

650 6.1 Prestressed stayed columns

651 Prestressed stayed columns are important elements of many modern large-scale structures; see Figure 15.
 652 Such columns tend to be slender and have intermediately placed cross-arms and associated pretensioned
 653 cables, thereby reducing the buckling effective length L_e . The length L_e provides a measure of the critical
 654 buckling eigenmode wavelength and the Euler strut buckling load is proportional to $1/L_e^2$. The system of
 655 cable stays and cross-arms in the prestressed stayed columns provide intermediate restraints that reduce L_e
 656 significantly and hence provide a commensurate increase in critical buckling load and ultimate capacity.
 657 Depending on the overall geometry, this change in critical buckling load can also be associated with
 658 quantitative and qualitative changes in the triggered buckling mode within the nonlinear range. The
 659 behaviour has been discussed at length in previous work, with the focus falling on qualitative critical
 660 [83] and post-buckling behaviour determined by the pretensioning force [84], physical experiments [85],
 661 triggering of modal interactions and associated symmetry-breaking [86, 59] and tuning behaviour for
 662 different cases [87, 88].

663 Some of these works use conventional finite element modelling, where post-buckling shapes are initiated
 664 by introducing imperfections that are affine to linear buckling modes. A drawback is that the full picture
 665 of modal interaction only becomes available under a combination of symmetric and anti-symmetric
 666 imperfections. Other modes may also be drawn in, for example, should it be thin enough, localised buckling
 667 in the main tubular column, and the numerical methodology discussed in Section 3.3, can be useful.
 668 Nevertheless, there has been a sequence of increasingly-sophisticated low-dimensional models, to capture



Figure 15. Prestressed stayed columns in practice. Left to right: an example as a slender support for a façade in Chiswick Park, West London; a set of roof supports in the former Eurostar terminal in Waterloo Station in Central London; an example in a shopping mall in Dalian, China. Photographs courtesy of Dr Daisuke Saito and Dr Jialiang Yu.

669 mode interaction [89, 59]. These models are based on the Rayleigh–Ritz method, with a finite number
 670 of linear eigenmodes of the unstayed column being used to discretise the deformation response, with
 671 cross-arms acting as beams, and cable stays as tension-only members.

672 The particular complication in stayed columns is produced by the cable stay, where there is the possibility
 673 of a sudden loss in elastic stiffness caused by cables slackening. The outcome is similar to that described
 674 in Figures 2(d) and 3(c). Using numerical continuation it has been possible to track post-buckling paths
 675 of perfect systems within the package AUTO-07P [45]. Figure 16 shows a realistically-proportioned
 676 symmetric stayed column system of length L with three cross-arms of lengths a_e and a_m , the exact details
 677 of which are presented in [59]. It shows that the mechanical response is likely to destabilise when distinct
 678 modes are triggered or mode interaction dominates; the kinks in the post-buckling paths are signatures of
 679 the portions of the cable stays going slack, instantly losing axial stiffness, and causing a sudden unstable
 680 jump in the response.

681 The column subsequently restabilises once it finds a configuration that restores equilibrium. Both the
 682 numerical continuation procedure for the analytical model, and the Riks algorithm used in ABAQUS, can
 683 capture this behaviour. One advantage of the former is that it tends to crystallise the detailed mechanical
 684 response into a few distinctive characteristics; the main column buckling modes are discretised into a
 685 Rayleigh–Ritz type model, and the nonlinear results provide straightforward output of the contributions of
 686 the linear buckling modes to the post-buckling profile, Q_1 and Q_2 being amplitudes of the first two main
 687 column buckling modes. This analysis allows the interpretation of the effects of symmetry-breaking, and
 688 the potential to trigger higher pure or interactive modes in the post-buckling range.

689 All the consequences for the post-critical strength, stiffness and potential to jump between different
 690 equilibrium states owing to the cable stay behaviour, can be determined directly. This information can

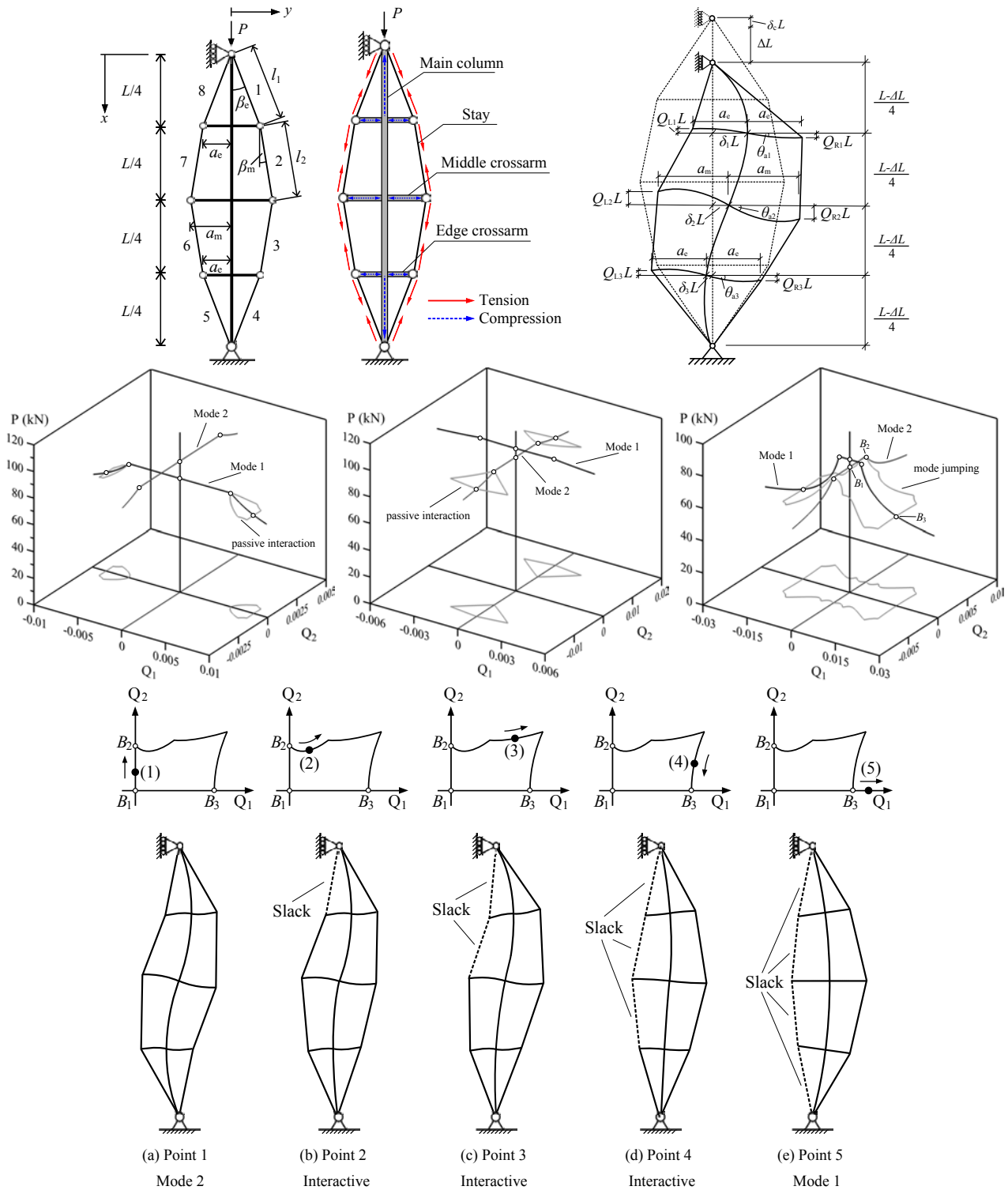


Figure 16. Prestressed stayed column. (Row 1: left to right) **Geometric definitions; effect of prestressing and buckled shape showing deformations of main column, cross-arms and stays used in the Rayleigh–Ritz model.** (Row 2: left to right) **Equilibrium paths showing: distinct mode 1 buckling (Q_1); distinct mode 2 buckling (Q_2); interactive buckling with a secondary mode jumping path.** (Rows 3–4) **Illustration of mode jumping through different points on the secondary mode jumping path from the third case in row 2 now plotted as Q_1 versus Q_2 in row 3 and the deformed structure presented in row 4.**

691 then be used to determine parametric spaces where practical geometric quantities such as stay diameter,
 692 layout of the stayed column system and initial prestressing forces, can generate qualitatively different, yet
 693 predictable, responses [59, 87], as shown in Figure 16.

694 The simplest configuration with a single-cross arm can also be considered as a single cell within a larger
 695 lattice material. The performance of metal lattices, for example with a criss-cross structure as in [90], may
 696 be enhanced by including internally woven tension ties, to make them similar to woven composites [91].
 697 The behaviour of the sandwich panel of Figure 17, depends on nonlinear interactions between the individual
 698 cells, and is observed to have a similar structure to the stayed column. By adjusting the pretension in the
 699 ties at the production stage, alongside the geometry of the cells and the overall configuration, it is possible
 700 to engineer the post-buckling stiffness to a desired level. If, for instance, the post-buckling stiffness of an
 overall panel can be tuned to be practically zero [92], but with each buckling cell having a significant critical

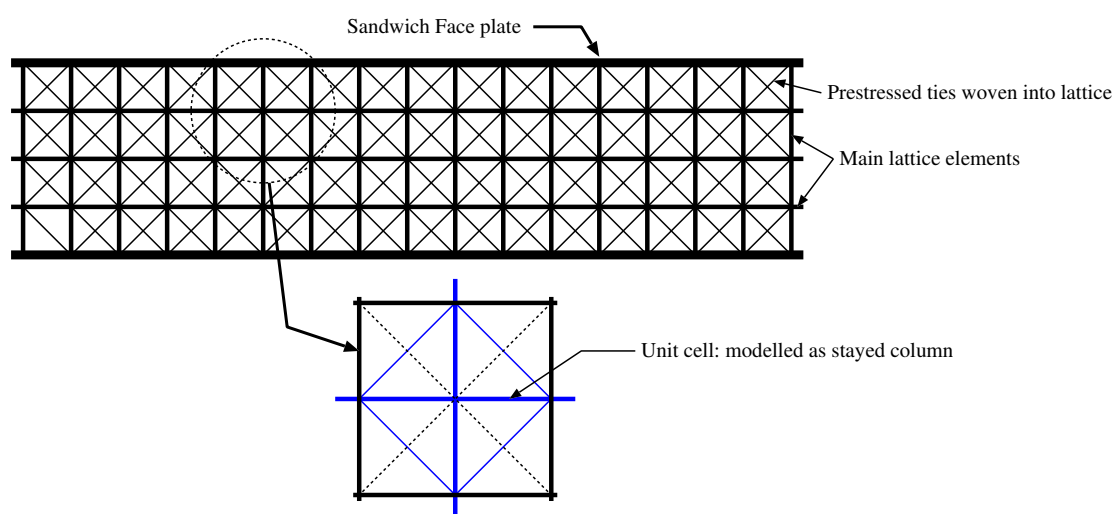


Figure 17. Sandwich panel with prestressed lattice core, the unit cells of which can be represented as prestressed stayed columns, as highlighted in the lower diagram [90, 91].

701 load, then the structure would be highly effective in absorbing energy. Moreover, since stress propagation
 702 depends on structural stiffness, if the post-buckling stiffness on the panel were zero, it would potentially
 703 minimise stress transfer to any attached structure. This type of application, using internal buckling of a
 704 lattice material for dynamic isolation purposes, has potential for applications where lightweight reusable
 705 elements are required for impact and blast protection or seismic isolation [93].
 706

707 6.2 Adaptive structures

708 So-called adaptive structures are able to change shape and/or material properties in response to varying
 709 external stimuli [94]. The application of adaptivity in engineering has the potential for significant
 710 improvements in performance, by making structures more efficient over a broad range of operating
 711 conditions [95]. A fascinating natural example of shape-adaptivity is the Venus flytrap, whose rapid
 712 transition from open to closed to capture its prey occurs as a consequence of snap-buckling instability [96].
 713 Hence, when operating conditions require large displacements and/or multiple stable configurations,
 714 structural instabilities can be viewed as potentially advantageous rather than a source of failure.

715 Consider for simplicity the buckling response of a simply-supported Euler strut, illustrated in Fig. 18. In
 716 particular, consider the stable post-buckled configuration in the inset of Figure 19(a). For given combinations

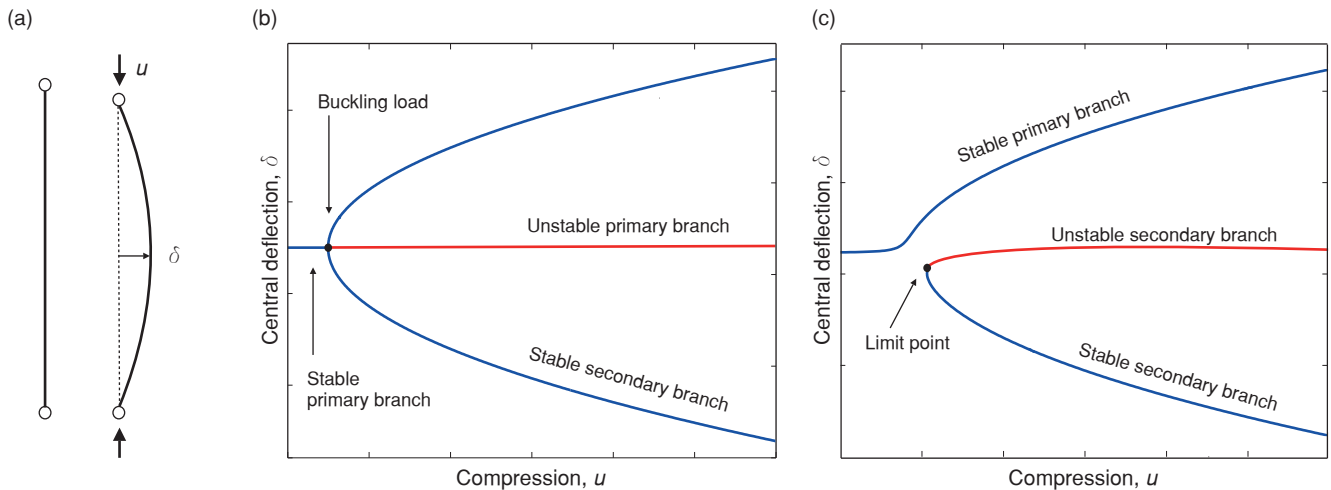


Figure 18. Buckling of a simply-supported strut and corresponding equilibrium diagrams. (a) The strut deflects sideways when subjected to a compressive force greater than the buckling load. (b) An idealised symmetric strut with no geometric or loading imperfections features a symmetric pitchfork bifurcation diagram in load vs displacement space. (c) Initial imperfections break the pitchfork.

717 of compression and symmetry-breaking defects, such a post-buckled structure can behave like an arch,
 718 exhibiting dynamic “snap-through” behaviour between the two stable states when subjected to an external
 719 transverse load, F . For a beam compressed just beyond the first buckling load, these configurations connect
 720 via an S-shaped equilibrium path in the space of a centrally-applied force, F plotted against the midpoint
 721 respective deflection δ , as shown graphically in Figure 19(a). The structure initially deflects in a stable
 722 manner before reaching a maximum limit point, where it snaps dynamically through a region of instability
 723 (2) onto the equilibrium branch for its second stable configuration (3).

724 Compression levels required to produce any meaningful shape-change from δ to $-\delta$ are typically sufficient
 725 to cause snap-through at a symmetry-breaking bifurcation (see asymmetric red shape in Figure 19(a)).
 726 Figure 19(b) shows how the equilibrium path in the F vs δ plane connects the two stable branches of the
 727 broken pitchfork. Figure 19(b) also shows how the limit points of the F vs δ equilibrium path change as a
 728 function of the compressive displacement, u , via the black fold line.

729 Specifically, the fold line tracks the two limit points with respect to changes in the compressive
 730 displacement, u , thereby illustrating the border between stable and unstable equilibria. By reducing
 731 u , the two limit points of the equilibrium path in Figure 19(a) collide in a cusp singularity. This cusp
 732 singularity therefore determines the critical value of compression, u , at the onset of dynamic snap-through
 733 behaviour [97]. Indeed, depending on the value of compression, u , three distinct types of post-buckling
 734 behaviour can be observed when the transverse load, F , is applied:

- 735 1. For values of compression, u , greater than the limit point on the broken-away pitchfork branch, the
 736 structure snaps from its first stable shape to its second configuration, traversing the region of instability
 737 delimited by the fold line. A self-equilibrated second configuration exists (stable even when F is
 738 removed). The structure is said to be bistable.
- 739 2. Reducing the compression, u , into the region between the limit point on the broken-away pitchfork
 740 branch and the cusp singularity, allows the beam to traverse a region of instability when F is applied,
 741 thereby still exhibiting snap-through behaviour. However, at these values of compression, it does not

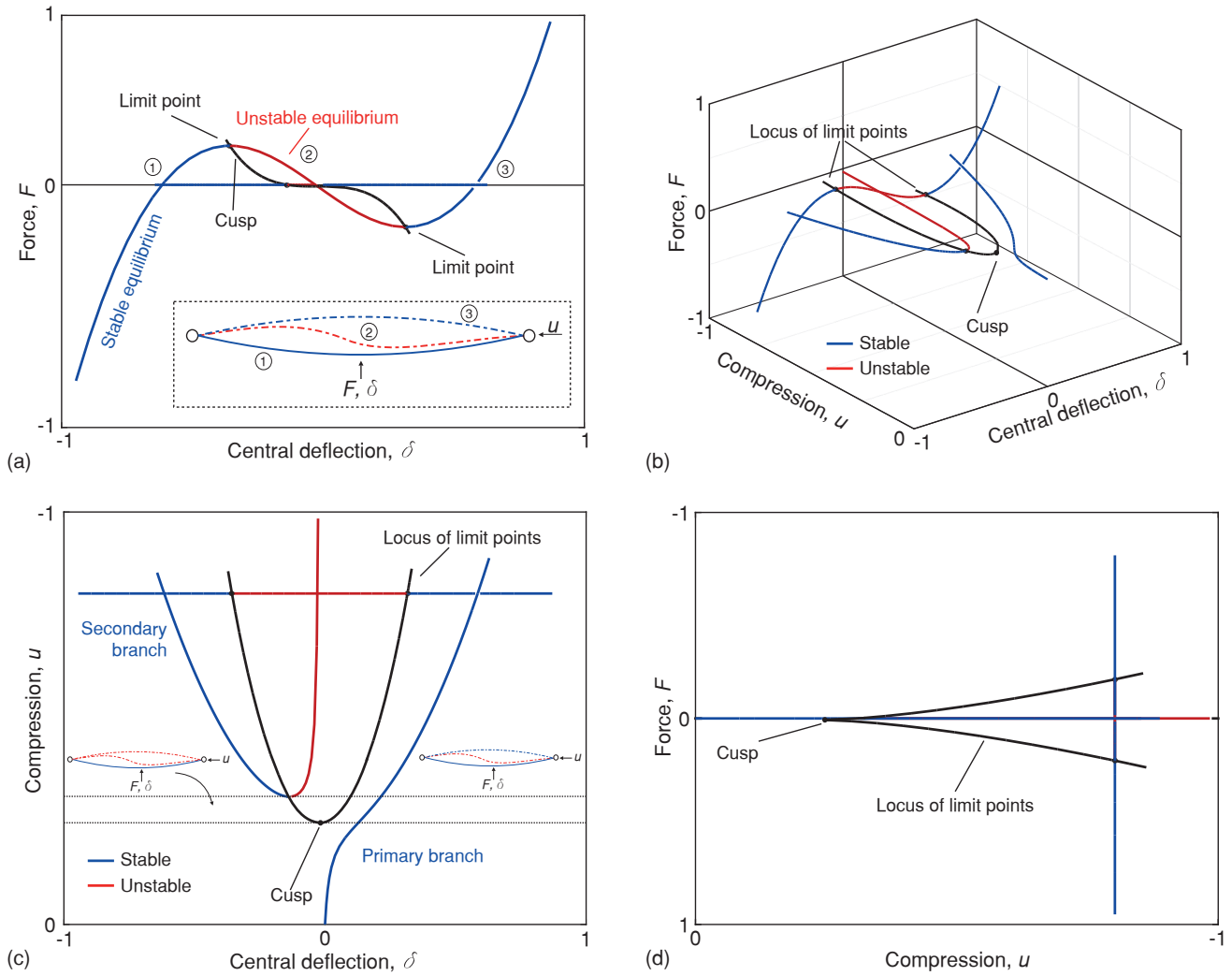


Figure 19. (a) Equilibrium path of force (F) vs central deflection (δ). (b) Compression-central deflection-force space showing a broken pitchfork and the locus of limit points of the snap-through curve. Panels (c) and (d) show the locus of limits point in central deflection-compression and compression-force space, respectively.

- 742 have a second stable configuration for $F = 0$. When the external force is removed, the strut then snaps
 743 back to its primary state. In other words it shows “super-elastic” monostability.
- 744 3. By decreasing the level of compression, u , even further the structure deforms nonlinearly, displaying
 745 stiffness adaptation but without snap-through. It is then elastically monostable or simply stable.

746 The control of geometrical parameters, material properties and/or boundary conditions can be used to tailor
 747 the equilibrium manifolds and adapt the multistability of the system to specific working and environmental
 748 conditions. We now consider a practical example.

749 A passive adaptive air inlet can regulate the opening aperture of a connected duct by interacting with
 750 the fluid flow around it. As shown in Figure 20, the inlet comprises a deformable, glass-fibre panel poised
 751 in an open state. The panel has been buckled into the region between the limit point of the broken-away
 752 branch and the cusp (refer to the taxonomy above), making it monostable.

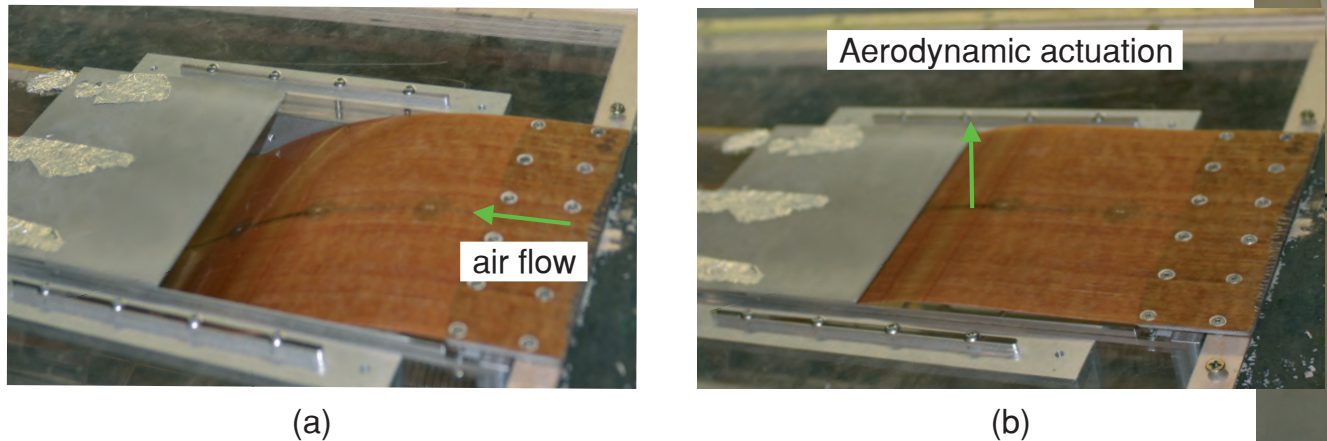


Figure 20. Adaptive air inlet demonstrator. (a) Open state. (b) Closed configuration.

753 As the airflow streaming over the panel accelerates into the connected duct, the decreasing pressure field
 754 creates an upwards force on the panel causing it to snap shut at a critical airspeed. If the airspeed is lowered
 755 beneath another threshold, the inlet automatically opens again. Unlike traditional shape-changing systems,
 756 the inlet does not rely on auxiliary devices for actuation. By increasing the amount of compression beyond
 757 the limit point on the broken-away path, the inlet can be transformed into a bistable structure that remains
 758 closed once the airflow is reduced. The greater the applied compression, the higher the airspeed required to
 759 actuate snap-through; the system's parameters can be tailored to meet specific operating requirements (see
 760 [98, 99] for further details).

761 This device has potential for engineering applications where cooling and drag reduction create competing
 762 design drivers. Examples include air inlets on cars or cooling ducts on jet engines, which use fresh-air
 763 cooling for reliable engine operation although this cooling induces a drag penalty. For additional engineering
 764 examples that use the nonlinear taxonomy described above, see *e.g.* [100, 101, 102, 103, 104, 105, 106, 107]
 765 and references therein.

766 **6.3 Buckling-induced auxetic materials**

767 The fact that materials exist with negative Poisson's ratio is not only intriguing but also of practical
 768 significance. So-called *auxetic materials* typically exhibit high energy absorption and fracture resistance,
 769 and have a broad range of practical applications from blast curtains and shock absorbers to running
 770 trainers and the ability to control waves (see for example [108, 109, 110, 111, 112, 113] and references
 771 therein). Auxetic materials are known to occur naturally (various honeycomb structures for instance or
 772 even crumpled paper [113] but with recent technological advances in 3D printing they can also be readily
 773 manufactured. This ease of manufacture opens exciting new opportunities to tailor such materials, and
 774 work has exploded in this area. To show something of the flavour of this exciting new field, we now
 775 briefly outline two examples of auxetic behaviour studied recently by the present authors, induced by local
 776 instabilities within the material's structure.

777 Experimental and numerical work led by Bertoldi et al. [111] has demonstrated how mechanical
 778 instabilities in periodic porous structures can lead to the dramatic reorganisation of the material from
 779 the original configuration, giving rise to the auxetic possibilities. One widely studied structure involves
 780 the uni-axial loading of a square array of circular holes made of an elastomeric matrix, which can be
 781 readily manufactured using a 3D printer. The hexagonally-shaped sample shown in Fig. 21 at the right is

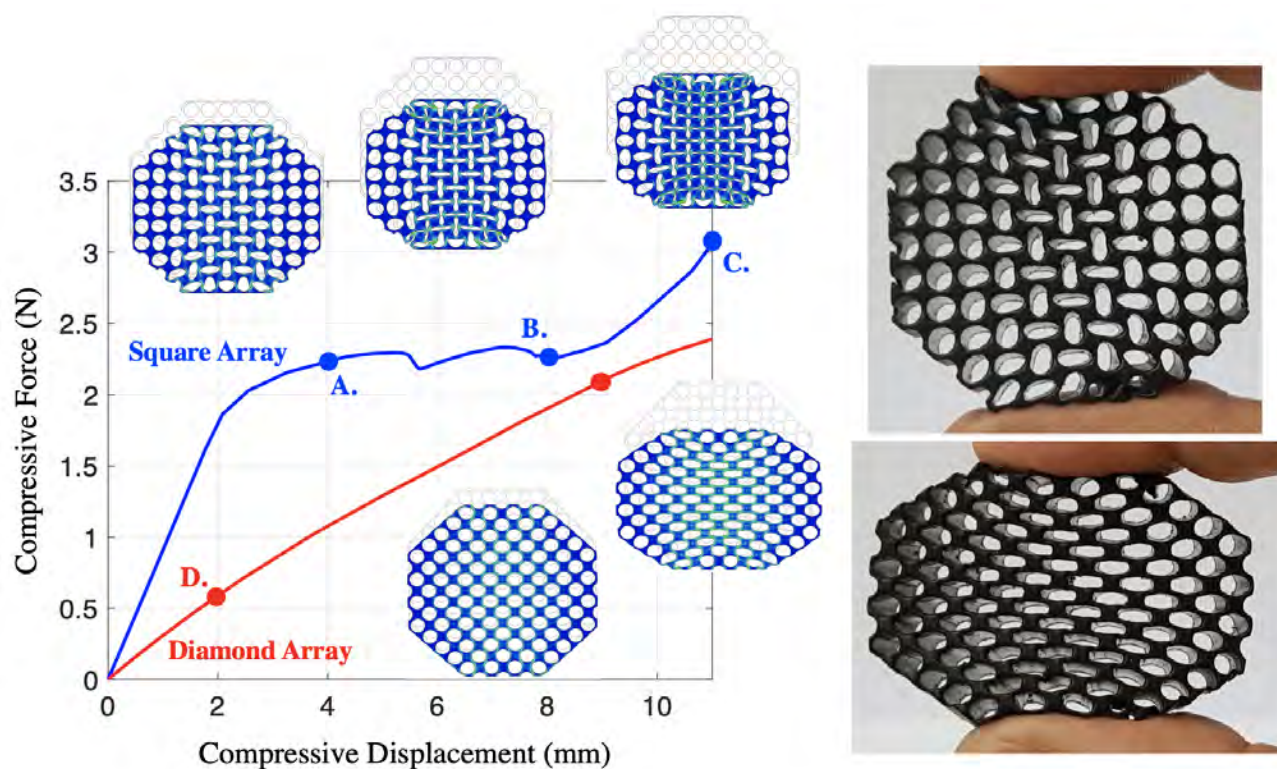


Figure 21. (Left) Shows 2D simulations of hexagonal lattices under different configurations (square and diamond) using ABAQUS. The geometry is discretised with 40,000 triangular elements, and model as linear elastic material under large deformation, strain and contact. (Right) Shows manufactured specimens in each of the configurations.

782 manufactured with an OBJET Connex 3D printer (Stratasys Ltd., USA), a machine that employs PolyJet
 783 Matrix Technology to dispense material—in this case *Tango*, a rubber-like elastomer—from designated
 784 micro-scale inkjet printing nozzles [114, 115]. When a compressive load is aligned with the square
 785 array, geometric reorganisation is seen, as the elastic instability induces periodic deformation patterns
 786 of tessellating ∞ -shaped voids. At the macroscale, this generates a nonlinear auxetic response by the
 787 simulations shown in blue in Fig. 21. Interestingly if our hexagonal specimen is rotated through 45° degrees,
 788 so that the compressive load acts on a diamond arrangement of circular holes, the material response is close
 789 to that of classical linear elastic (non-auxetic) material (red line).

790 Most examples of auxetic behaviour in the literature are based on re-entrant structures [116, 108, 109,
 791 113], and we next briefly review a recent contribution [117] detailing a variant that allows phase transitions
 792 from auxetic to non-auxetic phases and vice versa, based on the unit cell shown in Fig. 22. The cell
 793 comprises two back-to-back single degree-of-freedom arches with displacements measured by Q_1 and
 794 Q_2 , linked by the linear spring of stiffness k [118], and has the load to end-displacement response shown
 795 in Fig. 23(b). The continuous smooth curve replicates the response of a single arch [118], apart from
 796 the fact that under displacement control it goes unstable at bifurcation point A. Here the stable post-
 797 buckling solution becomes non-homogeneous, with displacement in one of the arches outpacing the other.
 798 This asymmetry continues until the first component passes through the horizontal and begins to stiffen,
 799 whereupon displacement in the other starts to take over. Symmetry is again restored at bifurcation B.

800 The absence of homogeneity in the natural loading path gives the potential for considerable complexity
 801 of response once cells are combined, as in Fig. 24. The responses are shown in Fig. 25. With a relatively

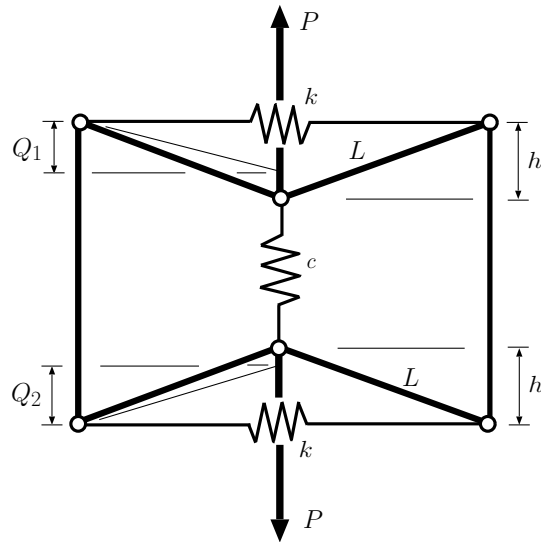


Figure 22. A new model for an auxetic cell, depicted in the the unloaded state where $P = 0$ and $Q_1 = Q_2 = h$. The illustrated auxetic configuration becomes non-auxetic once the arms have passed through horizontal. Typically, the arches snap through in turn rather than simultaneously.

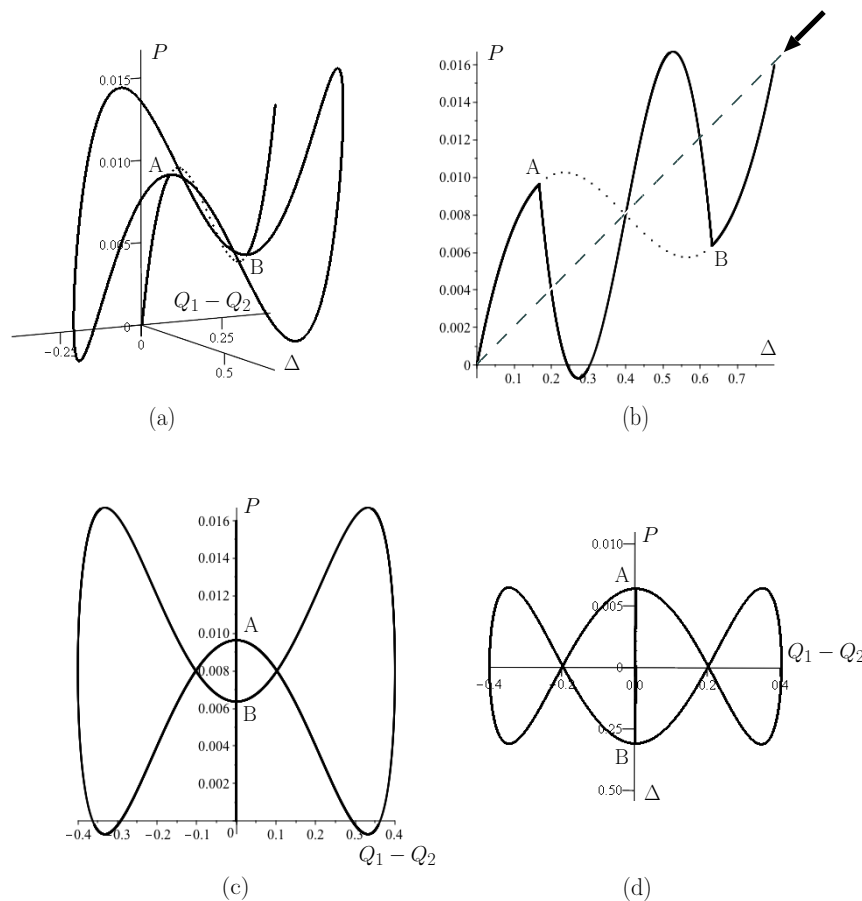


Figure 23. Response of the cell of Fig.22 for $L = 1$, $h = 0.2$, $k = 1$ and $c = 0.02$. Solid line depict stable equilibrium states under controlled stretch Δ , and the dotted line unstable states. (a) Three-dimensional plot of load P against its corresponding deflection $\Delta = 2h - Q_1 - Q_2$, and the symmetry-breaking variable $(Q_1 - Q_2)$. (b) Projection onto the $P - \Delta$ plane. (c) Projection onto the $P - (Q_1 - Q_2)$ plane. (d) Projection onto plane perpendicular to the direction of the arrow in (b).

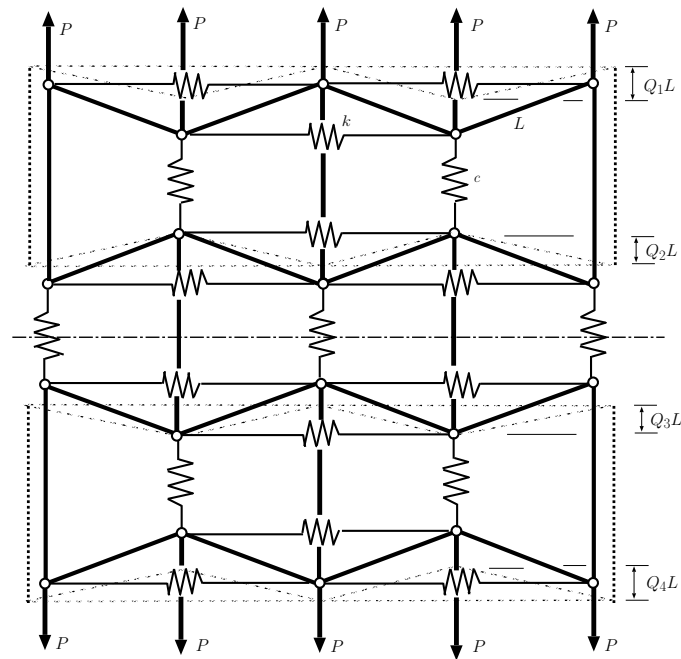


Figure 24. Combined cells of the form of Fig.22. With the centreline held stationary, displaced states are shown dashed. We refer to this configuration as a three-tier system, with four effective degrees-of-freedom $Q_i, i = 1..4$.

802 modest extension of the single cell model, a complex tangle of stable and unstable equilibrium paths is
 803 generated. Further details can be found in [117].

7 CONCLUSION

804 This theme issue focuses on the notion of stability in a variety of different contexts, both mathematical and
 805 practical. It could be argued that there is no more classical context in which one thinks of stability than
 806 structural engineering. It is fundamentally the job of the structural engineer to avoid buckling, failure or
 807 collapse. This paper takes a slightly different point of view on the topic. We focus on emerging ideas of
 808 elastic stability and post-instability behaviour of structures that fail subcritically, via irreversible jumps in
 809 energy. Such problems are of current interest for at least three reasons.

810 First and foremost, because of their sensitivity to shocks and imperfections, there is difficulty in certifying
 811 such structures for safety. We have argued that despite over 70 years since Koiter's pioneering work, a
 812 robust methodology for analysing the stability of such structures has yet to emerge. We have promoted
 813 here a promising line of attack, based on the Maxwell equal energy criterion and the concept of the
 814 mountain pass, as well as emerging ideas on how such ideas might be applied experimentally. However
 815 there remains much to be done before such ideas can provide a practical assessment and design tool. It
 816 is also interesting to note how the method relies on understanding the structure of unstable, localised
 817 postbuckling paths, which form the energy barriers or basin boundaries of the problem. In that sense,
 818 there is a strong connection to other active areas of stability-related research; tipping points in natural
 819 systems (see e.g. [119]), and transition to turbulence in pipe flow and related fluid-dynamic problems (see
 820 e.g. [120]).

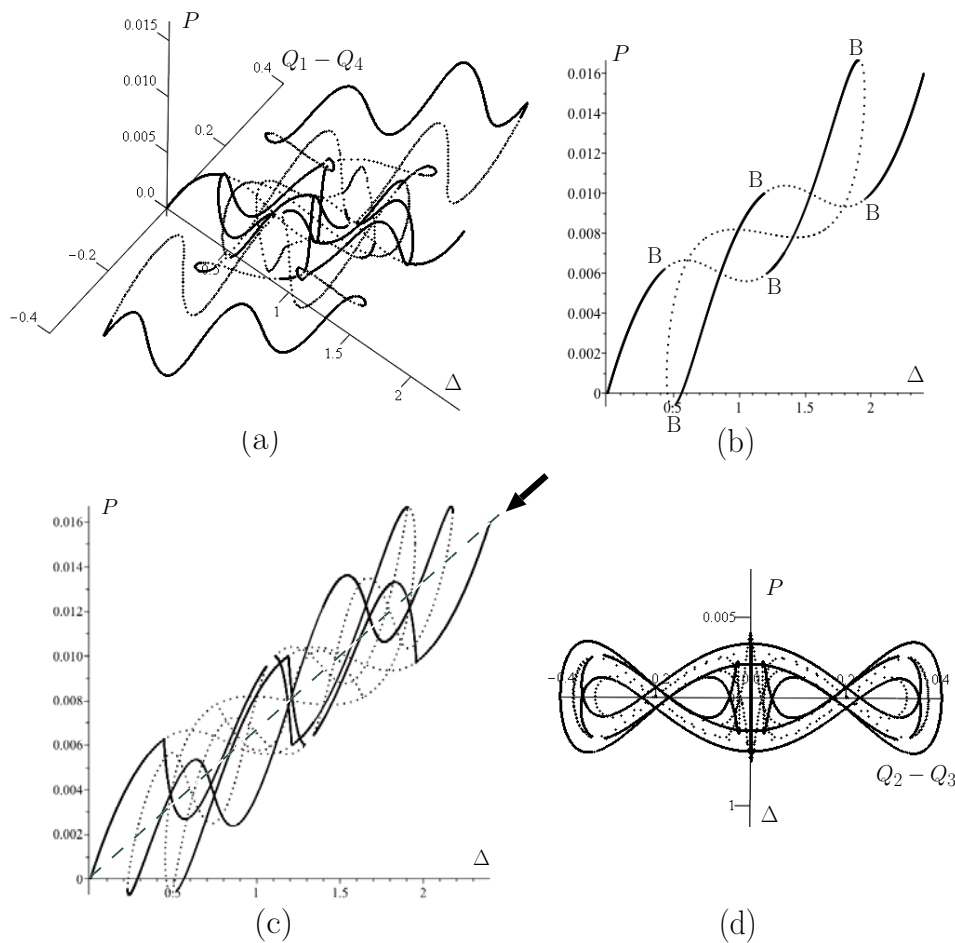


Figure 25. Response of the three-tier system of Fig. 24, for $L = 1$, $h = 0.2$, $k = 0.5$ and $c = 0.02$. (a) Load P plotted against its corresponding deflection Δ and the symmetry-breaking variable ($Q_1 - Q_4$). (b) Symmetric solutions for which $Q_1 = Q_4$ and $Q_2 = Q_3$. (c) Projection of (a) on to the $P - \Delta$ plane. (d) Projection on to plane perpendicular to the direction of the arrow in (c).

821 Second, the structural engineering domain is changing. Across numerous lengthscales, there is a quest
 822 for ever more lightweight structures. It could be said that the revolution in composites and other nano-
 823 structured materials has been threatening to revolutionise just about the whole of the built environment
 824 for almost 50 years. Yet, despite the huge investment within academia and industry, why are we not yet
 825 seeing carbon fibre motor cars come off the production line, wholly composite aeroplanes in our airports,
 826 or fibre-reinforced polymer buildings being constructed *en masse*? There are doubtless a range of reasons
 827 for this slow penetration of composite technologies, and as most disruptive technologies, the revolution
 828 may actually be just around the corner. Nevertheless, we would argue that one of the bottlenecks still to be
 829 overcome, is that we do not understand how such structures fail. Most lightweight structures are optimised
 830 for strength, but such optimisation typically leads to subcritical failure modes (see e.g. [28]). But, for
 831 structures made from composite materials, to the uncertainty and sensitivity of classical steel and concrete
 832 structures that buckle subcritically, we have additional complexities of anisotropy, internal micro-structural
 833 lengthscales and buried failures, cracks or delaminations that are hard to characterise and inspect. We have
 834 also seen, through the example of an auxetic material, that the distinction between materials and structures
 835 is fundamentally being blurred. It would seem then, the seeds of the robust methodology we have been
 836 trying to sow in this article are more important now than ever, if the true potential of nano-structured

837 materials is to be realised in the built environment. We hope that future researchers may be inspired to
838 water these seeds.

839 Finally, there is the point of view that we have been also trying to promote in this article that instability
840 is not necessarily a bad thing. We have highlighted three areas of possible engineering exploitation of
841 non-reversible structural instability. More generally though, we are quite used to the notion of things
842 that snap and pop into instability. These include the pressure required to depress the keys on a computer
843 keyboard being controlled by dome buckling, to old-fashioned bi-metallic strips being used to control
844 switches, as in a motor car indicator light. Crash barriers and crumple zones also exploit the idea that elastic
845 deformation of a subcritical structure can lead to transfer of significant amounts of energy into permanent
846 plastic deformation. Origami also provides an inspiration to engineers in how small energy barriers need
847 to be overcome in order to fold (or unfold) a structure into a new shape (see *e.g.* [121, 122, 123]). Most
848 interestingly, there is great potential to draw inspiration from biology. Irreversible transitions are the
849 norm in biology, for example in cell division, cell polarity formation and most morphogenesis problems.
850 Although such processes are often controlled by genes and other signaling proteins, there is an increasing
851 body of work that looks at the biomechanics of such transitions. Indeed, at many different lengthscales,
852 processes that are crucial to development, or to the maintenance of an organism or ecosystem require
853 sudden, irreversible response to continuous variation of external conditions. It is easy to think of examples
854 like the springing of a Venus fly trap, or the opening of seed pods that can easily be regarded as buckling
855 events of the nature described in this paper.

856 Clearly, there remain many lessons that engineers and designers need to learn by taking inspiration from
857 the natural world. Not least among such lessons, as we seek to build a more resilient world in the face of
858 global change, must surely be that there need not necessarily be anything to fear from an instability. Not
859 only are sudden irreversible instabilities not necessarily to be feared, they can in fact be designed to be
860 exploited for the greater good. Happy catastrophes indeed!

FUNDING

861 T.J.D. is funded by the Alan Turing Institute under a Turing Fellowship [Grant No. EP/N510129/1].
862 R.M.J.G. is funded by the Royal Academy of Engineering under the Research Fellowship scheme [Grant
863 No. RF\201718\17178]. A.P. is funded by the UK Engineering and Physical Sciences Research Council
864 under an Early Career Research Fellowship [Grant No. EP/M013170/1]. R.M.N. is funded by the UK
865 Engineering and Physical Sciences Research Council [Grant No. EP/N509619/1].

ACKNOWLEDGMENTS

866 The authors acknowledge useful conversations with D. Avitabile, G.J. Lord, J. Sieber and J.M.T. Thompson.

SUPPLEMENTAL DATA

867 There is none.

DATA AVAILABILITY STATEMENT

868 No new experimental data is presented in this paper.

REFERENCES

- 869 [1] Budiansky B, Hutchinson JW. Buckling: progress and challenge. Besseling JF, van der Heijden
870 AMJ, editors, *Trends in Solid Mechanics 1979. Proceedings of the symposium dedicated to the 65th*
871 *birthday of W. T. Koiter* (Delft University Press) (1979).
- 872 [2] Hutchinson JW, Thompson JMT. Imperfections and energy barriers in shell buckling. *Int. J. Solids*
873 *Struct.* **148** (2018) 157–168.
- 874 [3] Reis PM. A perspective on the revival of structural (in)stability with novel opportunities for function:
875 From buckliphobia to buckliphilia. *J. Appl. Mech. – Trans. ASME* **82** (2015) 111001.
- 876 [4] Zeeman EC. Catastrophe theory. *Sci. Am.* **April** (1976) 65–70, 75–83.
- 877 [5] Thompson JMT. Catastrophe theory in mechanics: progress or digression. *J. Struct. Mech.* **10**
878 (1982) 167–175.
- 879 [6] Wadee MA, Champneys AR. Fail safe or fail dangerous? Parc S, editor, *50 visions of mathematics*
880 (London: Oxford University Press), chap. 44 (2014), 163–167.
- 881 [7] Thompson JMT, Hunt GW. *A general theory of elastic stability* (London: John Wiley & Sons)
882 (1973).
- 883 [8] Arbocz J, Ho JMAM. Collapse of axially compressed cylindrical shells with random imperfections.
884 *AIAA J.* **29** (1991) 2247–2256.
- 885 [9] Elishakoff I, Li Y, Starnes Jr JH. *Nonclassical problems in the theory of elastic stability* (Cambridge:
886 Cambridge University Press) (2001).
- 887 [10] Croll JGA, Batista RC. Explicit lower bounds for the buckling of axially loaded cylinders. *Int. J.*
888 *Mech. Sci.* **23** (1981) 331–343.
- 889 [11] Thompson JMT, Sieber J. Shock-sensitivity in shell-like structures: With simulations of spherical
890 shell buckling. *Int. J. Bifurcation Chaos* **26** (2015) 1630003.
- 891 [12] Kreilos T, Schneider TM. Fully localized post-buckling states of cylindrical shells under axial
892 compression. *Proc. R. Soc. A – Math. Phys. Eng. Sci.* **473** (2017) 20170177.
- 893 [13] Koiter WT. *On the stability of elastic equilibrium*. Ph.D. thesis, Technische Hogeschool, Delft
894 (Technological University of Delft), The Netherlands (1945). English translation issued as NASA,
895 *Tech. Trans.*, **F 10**, 833, 1967.
- 896 [14] Riks E. An incremental approach to the solution of snapping and buckling problems. *Int. J. Solids*
897 *Struct.* **15** (1979) 529–551.
- 898 [15] Crisfield MA. A fast incremental/iterative solution procedure that handles “snap-through”. *Comput.*
899 *Struct.* **13** (1981) 55–62.
- 900 [16] Doedel EJ, Champneys AR, Fairgrieve TF, Kuznetsov YA, Sandstede B, Wang X. *AUTO 97:*
901 *Continuation and bifurcation software for ordinary differential equations (with HomCont)* (1998).
- 902 [17] Eriksson A. Structural instability analyses based on generalised path-following. *Comput. Meth.*
903 *Appl. Mech. Eng.* **156** (1998) 45–74.
- 904 [18] Groh RMJ, Avitabile D, Pirrera A. Generalised path-following for well-behaved nonlinear structures.
905 *Comput. Meth. Appl. Mech. Eng.* **331** (2018) 394–426.
- 906 [19] Castro SGP, Zimmermann R, Arbelo MA, Khakimova R, Hilburger MW, Degenhardt R. Geometric
907 imperfections and lower-bound methods used to calculate knock-down factors for axially
908 compressed composite cylindrical shells. *Thin-Walled Struct.* **74** (2014) 118–132.
- 909 [20] Lee A, López Jiménez F, Marthelot J, Hutchinson JW, Reis PM. The geometric role of precisely
910 engineered imperfections on the critical buckling load of spherical elastic shells. *J. Appl. Mech. –*
911 *Trans. ASME* **83** (2016) 111005.

- 912 [21] Hunt GW, Peletier MA, Champneys AR, Woods PD, Wade MA, Budd CJ, et al. Cellular buckling
 913 in long structures. *Nonlinear Dyn.* **21** (2000) 3–29.
- 914 [22] Riks E. The application of Newton’s method to the problem of elastic stability. *J. Appl. Mech. –*
 915 *Trans. ASME* **39** (1971) 1060–1065.
- 916 [23] Hunt GW. An algorithm for the nonlinear analysis of compound bifurcation. *Phil. Trans. R. Soc. A*
 917 *– Math. Phys. Eng. Sci.* **300** (1981) 443–471.
- 918 [24] Koiter WT. The nonlinear buckling problem of a complete spherical shell under uniform external
 919 pressure. *Proc. Kon. Ned. Ak. Wet.* **B72** (1969) 40–123.
- 920 [25] Budd CJ, Hunt GW, Kuske R. Asymptotics of cellular buckling close to the Maxwell load. *Proc. R.*
 921 *Soc. A – Math. Phys. Eng. Sci.* **457** (2001) 2935–2964.
- 922 [26] Kerr AD. On thermal buckling of of straight railroad tracks and the effect of track length on track
 923 response. *Rail Int.* **9** (1979) 759–768.
- 924 [27] Wade MA, Hunt GW, Peletier MA. Kink band instability in layered structures. *J. Mech. Phys.*
 925 *Solids* **52** (2004) 1071–1091.
- 926 [28] Hunt GW. Reflections and symmetries in space and time. *IMA J. Appl. Math* **76** (2011) 2–26.
- 927 [29] Zhu E, Mandal P, Calladine CR. Buckling of thin cylindrical shells: An attempt to resolve a paradox.
 928 *Int. J. Mech. Sci.* **44** (2002) 1583–1601.
- 929 [30] Elishakoff I. Probabilistic resolution of the twentieth century conundrum in elastic stability.
 930 *Thin-Walled Struct.* **59** (2012) 35–57.
- 931 [31] Yamaki N. *Elastic stability of circular cylindrical shells* (Elsevier) (1984).
- 932 [32] Hunt GW, Bolt HM, Thompson JMT. Structural localization phenomena and the dynamical
 933 phase-space analogy. *Proc. R. Soc. A – Math. Phys. Eng. Sci.* **425** (1989) 245–267.
- 934 [33] Hunt GW, Lucena Neto E. Localized buckling in long axially-loaded cylindrical shells. *J. Mech.*
 935 *Phys. Solids* **39** (1991) 881–894.
- 936 [34] Hunt GW, Lord GJ, Champneys AR. Homoclinic and heteroclinic orbits underlying the post-
 937 buckling of axially-compressed cylindrical shells. *Comput. Meth. Appl. Mech. Eng.* **170** (1999)
 938 239–251.
- 939 [35] Horák J, Lord GJ, Peletier MA. Cylinder buckling: The mountain pass as an organizing center.
 940 *SIAM J. Appl. Math.* **66** (2006) 1793–1824.
- 941 [36] Hutchinson JW. Buckling of spherical shells revisited. *Proc. R. Soc. A – Math. Phys. Eng. Sci.* **472**
 942 (2016) 20160577.
- 943 [37] Beaty D. *A theoretical and experimental study of the stability of thin elastic spherical shells*. Ph.D.
 944 thesis, University of Michigan, USA (1962).
- 945 [38] Walker AC. An analytical study of the rotationally symmetric non-linear buckling of a complete
 946 spherical shell under external pressure. *Int. J. Mech. Sci.* **10** (1968) 695–710.
- 947 [39] Hunt GW, Lucena Neto E. Maxwell critical loads for axially loaded cylindrical shells. *J. Appl.*
 948 *Mech. – Trans. ASME* **60** (1993) 702–706.
- 949 [40] Hunt GW, Lord GJ, Peletier MA. Cylindrical shell buckling: a characterization of localization and
 950 periodicity. *Discrete Contin. Dyn. Syst. – Ser. B* **3** (2003) 505–518.
- 951 [41] Golubitsky M, Stewart I, Schaeffer D. *Singularities and groups in bifurcation theory*, vol. 2 (New
 952 York: Springer) (1998).
- 953 [42] Kuznetsov Y. *Elements of applied bifurcation theory* (New York: Springer), third edn. (2004).
- 954 [43] Haragus M, Iooss G. *Local bifurcations, center manifolds and normal forms in infinite-dimensional*
 955 *dynamical systems* (New York: Springer) (2011).

- 956 [44] Keller HB. *Lectures on numerical methods in bifurcation problems* (Berlin: Springer) (1986).
 957 Published for the Tata Institute of Fundamental Research.
- 958 [45] Doedel EJ, Oldeman BE. *AUTO-07P: Continuation and Bifurcation Software for Ordinary*
 959 *Differential Equations*. Concordia University, Montreal, Canada (2011).
- 960 [46] Sewell MJ. On the connection between stability and the shape of the equilibrium surface. *J. Mech.*
 961 *Phys. Solids* **14** (1966) 203–230.
- 962 [47] Ahmad S, Irons BM, Zienkiewicz OC. Analysis of thick and thin shell structures by curved finite
 963 elements. *Int. J. Numer. Methods Eng.* **2** (1970) 419–451.
- 964 [48] Reissner E. On the theory of bending of elastic plates. *J. Math. Phys.* **23** (1944) 184–191.
- 965 [49] Payette GS, Reddy JN. A seven-parameter spectral/hp finite element formulation for isotropic,
 966 laminated composite and functionally graded shell structures. *Comput. Meth. Appl. Mech. Eng.*
 967 (2014) 664–704.
- 968 [50] Bathe KJ. *Finite element procedures* (TBS), 1st edn. (2007), 577 .
- 969 [51] Pomeau Y. Front motion, metastability and subcritical bifurcations in hydrodynamics. *Physica D*
 970 **23** (1986) 3–11.
- 971 [52] Knobloch E. Spatial localization in dissipative systems. *Annu. Rev. Condens. Matter Phys.* **6** (2015)
 972 325–359.
- 973 [53] Groh RMJ, Pirrera A. On the role of localizations in buckling of axially compressed cylinders.
 974 *Proc. R. Soc. A – Math. Phys. Eng. Sci.* (2019) 20190006.
- 975 [54] Zeeman EC. *Catastrophe theory: Selected papers, 1972–1977* (Addison-Wesley, London) (1977),
 976 p. 53 .
- 977 [55] Wadee MA, Edmunds R. Kink band propagation in layered structures. *J. Mech. Phys. Solids* **53**
 978 (2005) 2017–2035.
- 979 [56] Wadee MA, Gardner L. Cellular buckling from mode interaction in I-beams under uniform bending.
 980 *Proc. R. Soc. A – Math. Phys. Eng. Sci.* **468** (2012) 245–268.
- 981 [57] Wadee MA, Bai L. Cellular buckling in I-section struts. *Thin-Walled Struct.* **81** (2014) 89–100.
- 982 [58] Bai L, Wang F, Wadee MA, Yang J. Nonlinear mode interaction in equal-leg angle struts susceptible
 983 to cellular buckling. *Proc. R. Soc. A – Math. Phys. Eng. Sci.* **473** (2017) 20170583.
- 984 [59] Yu J, Wadee MA. Mode interaction in triple-bay prestressed stayed columns. *Int. J. Non-Linear*
 985 *Mech.* **88** (2017) 47–66.
- 986 [60] Ambrosetti A, Rabinowitz PH. Dual variational methods in critical point theory and applications. *J.*
 987 *Funct. Anal.* **14** (1973) 349–381.
- 988 [61] Henkelman G, Uberuaga BP, Jónsson H. A climbing image nudged elastic band method for finding
 989 saddle points and minimum energy paths. *J. Chem. Phys.* **113** (2000) 9901.
- 990 [62] Henkelman G, Jónsson H. A dimer method for finding saddle points on high dimensional potential
 991 surfaces using only first derivatives. *J. Chem. Phys.* **111** (1999) 7010.
- 992 [63] Fischer A, Karplus M. Conjugate peak refinement—an algorithm for finding reaction paths and
 993 accurate transition-states in systems with many degrees of freedom. *Chem. Phys. Lett.* **194** (1992)
 994 252–261.
- 995 [64] Bonfanti S, Kob W. Methods to locate saddle points in complex landscapes. *J. Chem. Phys.* **147**
 996 (2017) 204104.
- 997 [65] Thompson JMT. Advances in shell buckling: Theory and experiments. *Int. J. Bifurcation Chaos* **25**
 998 (2015) 1530001.
- 999 [66] Lord GJ, Champneys AR, Hunt GW. Computation of homoclinic orbits in partial differential
 1000 equations: an application to cylindrical shell buckling. *SIAM J. Sci. Comput.* **21** (1999) 591–619.

- 1001 [67] Virost E, Kreilos T, Schneider TM, Rubinstein SM. Stability landscape of shell buckling. *Phys. Rev. Lett.* **119** (2017) 224101.
- 1002
- 1003 [68] Babcock CD, Sechler EE. The effect of initial imperfections on the buckling stress of cylindrical shells. Tech. Rep. NASA TN D-2005, California Institute of Technology (1963).
- 1004
- 1005 [69] Arbocz J. *The effect of general imperfections on the buckling of cylindrical shells*. Ph.D. thesis, California Institute of Technology, Pasadena, California, USA (1968).
- 1006
- 1007 [70] Tennyson RC. Buckling modes of circular cylindrical shells under axial compression. *AIAA J.* **7** (1969) 1481–1487.
- 1008
- 1009 [71] Hühne C, Rolfes R, Breitbach E, Teßler J. Robust design of composite cylindrical shells under axial compression — Simulation and validation. *Thin-Walled Struct.* **46** (2008) 947–962.
- 1010
- 1011 [72] Hilburger MW. On the development of shell buckling knockdown factors for stiffened metallic launch vehicle cylinders. *Proceedings of the 2018 AIAA/ASCE/AHS/ASC Structures, Structural Dynamics, and Materials Conference* (2018).
- 1012
- 1013
- 1014 [73] Wiebe R, Virgin LN. On the experimental identification of unstable static equilibria. *Proc. R. Soc. A – Math. Phys. Eng. Sci.* **472** (2016).
- 1015
- 1016 [74] Neville RM, Groh RMJ, Pirrera A, Schenk M. Shape control for experimental continuation. *Phys. Rev. Lett.* **120** (2018) 254101.
- 1017
- 1018 [75] Groh RMJ, Neville RM, Pirrera A, Schenk M. Virtual testing of experimental continuation. *ArXiv e-prints* (2018).
- 1019
- 1020 [76] Neville RM, Groh RMJ, Pirrera A, Schenk M. Quasi-static experimental path-following. *Proc. AIAA SciTech 2019* (2019). doi:10.2514/6.2019-0230.
- 1021
- 1022 [77] Eßlinger M, Geier B. Gerechnete Nachbeullasten als untere Grenze der experimentellen axialen Beullasten von Kreiszyklindern. *Der Stahlbau* **21** (1972) 353–360.
- 1023
- 1024 [78] Weingarten VI, Morgan EJ, Seide P. Elastic stability of thin-walled cylindrical and conical shells under axial compression. *AIAA J.* **3** (1965) 500–505.
- 1025
- 1026 [79] Degenhardt R, Kling A, Bethge A, Orf J, Kärger L, Zimmermann R, et al. Investigations on imperfection sensitivity and deduction of improved knock-down factors for unstiffened CFRP cylindrical shells. *Compos. Struct.* **92** (2010) 1939–1946.
- 1027
- 1028
- 1029 [80] Meurer A, Kriegesmann B, Dannert M, Rolfes R. Probabilistic perturbation load approach for designing axially compressed cylindrical shells. *Thin-Walled Struct.* **107** (2016) 648–656.
- 1030
- 1031 [81] Wang B, Hao P, Li G, Fang Y, Wang X, Zhang X. Determination of realistic worst imperfection for cylindrical shells using surrogate model. *Struct. Multidiscip. Optim.* **48** (2013) 777–794.
- 1032
- 1033 [82] Fan H. Critical buckling load prediction of axially compressed cylindrical shell based on non-destructive probing method. *Thin-Walled Struct.* **139** (2019) 91–104.
- 1034
- 1035 [83] Hafez HH, Temple MC, Ellis JS. Pretensioning of single-crossarm stayed columns. *J. Struct. Div. – ASCE* **105** (1979) 359–375.
- 1036
- 1037 [84] Saito D, Wadee MA. Post-buckling behaviour of prestressed steel stayed columns. *Eng. Struct.* **30** (2008) 1224–1239.
- 1038
- 1039 [85] Osofero AI, Wadee MA, Gardner L. Experimental study of critical and post-buckling behaviour of prestressed stayed columns. *J. Constr. Steel. Res.* **79** (2012) 226–241.
- 1040
- 1041 [86] Saito D, Wadee MA. Numerical studies of interactive buckling in prestressed steel stayed columns. *Eng. Struct.* **31** (2009) 432–443.
- 1042
- 1043 [87] Yu J, Wadee MA. Optimal prestressing of triple-bay prestressed stayed columns. *Structures* **12** (2017) 132–144.
- 1044

- 1045 [88] Lapira L, Wade MA, Gardner L. Stability of multiple-crossarm prestressed stayed columns with
 1046 additional stay systems. *Structures* **12** (2017) 227–241.
- 1047 [89] Wade MA, Gardner L, Hunt TA. Buckling mode interaction in prestressed stayed columns. *Proc.*
 1048 *Inst. Civil Eng. – Struct. Build.* **166** (2013) 403–412.
- 1049 [90] Queheillalt DT, Wadley HNG. Cellular metal lattices with hollow trusses. *Acta Mater.* **53** (2005)
 1050 303–313.
- 1051 [91] Zschoernack C, Wade MA, Völlmecke C. Nonlinear buckling of fibre-reinforced unit cells of lattice
 1052 materials. *Compos. Struct.* **136** (2016) 217–228.
- 1053 [92] Schenk M, Guest SD. On zero stiffness. *Proc. Inst. Mech. Eng. Part C – J. Mech. Eng. Sci.* **228**
 1054 (2014) 1701–1714.
- 1055 [93] Virgin LN, Davis RB. Vibration isolation using buckled struts. *J. Sound Vibr.* **260** (2003) 965–973.
- 1056 [94] Thill C, Etches J, Bond I, Potter K, Weaver PM. Morphing skins. *Aeronaut. J.* **112** (2008) 117–139.
- 1057 [95] Sun J, Guan Q, Liu Y, Leng J. Morphing aircraft based on smart materials and structures: A
 1058 state-of-the-art review. *J. Intell. Mater. Sys. Struct.* **27** (2016) 2289–2312.
- 1059 [96] Forterre Y, Skotheim J, Dumais J, Mahadevan L. How the venus flytrap snaps. *Nature* **433** (2005)
 1060 421–425.
- 1061 [97] Danso LA, Karpov EG. Cusp singularity-based bistability criterion for geometrically nonlinear
 1062 structures. *Extreme Mech. Lett.* **13** (2017) 135–140.
- 1063 [98] Arena G, Groh RMJ, Brinkmeyer A, Theunissen R, Weaver PM, Pirrera A. Adaptive compliant
 1064 structures for flow regulation. *Proc. R. Soc. A – Math. Phys. Eng. Sci.* **473** (2017) 20170334.
- 1065 [99] Arena G, Groh RMJ, Theunissen R, Weaver PM, Pirrera A. Design and testing of a passively
 1066 adaptive inlet. *Smart Mater. Struct.* **27** (2018) 085019.
- 1067 [100] Kebabze E, Guest SD, Pellegrino S. Bistable prestressed shell structures. *Int. J. Solids Struct.* **41**
 1068 (2004) 2801–2820.
- 1069 [101] Diaconu CG, Weaver PM, Mattioni F. Concepts for morphing airfoil sections using bi-stable
 1070 laminated composite structures. *Thin-Walled Struct.* **46** (2008) 689–701.
- 1071 [102] Mattioni F, Weaver PM, Friswell M. Multistable composite plates with piecewise variation of
 1072 lay-up in the planform. *Int. J. Solids Struct.* **46** (2009) 151–164.
- 1073 [103] Kuder IK, Arrieta AF, Raither WE, Ermanni P. Variable stiffness material and structural concepts
 1074 for morphing applications. *Prog. Aerosp. Sci.* **63** (2013) 33–55.
- 1075 [104] Arrieta A, Bilgen O, Friswell MI, Ermanni P. Modelling and configuration control of wing-shaped
 1076 bi-stable piezoelectric composites under aerodynamic loads. *Aerosp. Sci. Technol.* **29** (2013)
 1077 453–461.
- 1078 [105] Terwagne D, Brojan M, Reis PM. Smart morphable surfaces for aerodynamic drag control. *Adv.*
 1079 *Mater.* **26** (2014) 6608–6611.
- 1080 [106] Emam S, Inman D. A review on bistable composite laminates for morphing and energy harvesting.
 1081 *Appl. Mech. Rev.* **67** (2015) 060803.
- 1082 [107] Zirbel SA, Tolman KA, Trease BP, Howell LL. Bistable mechanisms for space applications. *PLoS*
 1083 *ONE* **11** (2016) e0168218.
- 1084 [108] Evans KE, Alderson A. Auxetic materials: functional materials and structures from lateral thinking.
 1085 *Adv. Mater.* **12** (2000) 617–628.
- 1086 [109] Evans KE, Alderson KL. Auxetic materials: the positive side of being negative. *Eng. Sci. Edu. J.* **9**
 1087 (2000) 148–154.
- 1088 [110] Evans KE, Nkansah MA, Hutchinson IJ, Rogers SC. Molecular network design. *Nature* **353** (1991)
 1089 124.

- 1090 [111] Bertoldi K, Reis PM, Willshaw S, Mullin T. Negative poisson's ratio behaviour induced by an
 1091 elastic instability. *Adv. Mater.* **22** (2010) 361–366.
- 1092 [112] Overvelde JTB, Shan S, Bertoldi K. Compaction through buckling in 2D periodic, soft and porous
 1093 structures: effect of pore shape. *Adv. Mater.* **24** (2012) 2337–2342.
- 1094 [113] Yang W, Li ZM, Shi W, Xie BH, Yang MB. Review on auxetic materials. *J. Mater. Sci.* **39** (2004)
 1095 3269–3279.
- 1096 [114] Stratasys. Polyjet multi-material 3d printing. Tech. rep., Stratasys (2015).
- 1097 [115] Sakhaei AH, Kaijima S, Lee TL, Tan YY, Dunn ML. Design and investigation of a multi-material
 1098 compliant ratchet-like mechanism. *Mech. Mach. Theory* **121** (2018) 184–197.
- 1099 [116] Lakes RS. Foam structures with a negative Poisson's ratio. *Science* **235** (1987) 1038–1040.
- 1100 [117] Hunt GW, Dodwell TJ. Complexity in phase transforming pin-jointed auxetic lattices. *Proc. R. Soc.*
 1101 *A – Math. Phys. Eng. Sci.* (2019). In Press.
- 1102 [118] Thompson JMT, Hunt GW. *Elastic instability phenomena* (Chichester: John Wiley & Sons) (1984).
- 1103 [119] Thompson JMT, Sieber J. Climate tipping as a noisy bifurcation: a predictive technique. *IMA J.*
 1104 *Appl. Math.* **76** (2011) 27–46.
- 1105 [120] Kerswell R. Recent progress in understanding the transition to turbulence in a pipe. *Nonlinearity*
 1106 **18** (2005) R17.
- 1107 [121] Schenk M, Guest SD. Geometry of miura-folded metamaterials. *Proc. National Academy of*
 1108 *Sciences* **110** (2013) 3276–3281.
- 1109 [122] Silverberg J, Evans AA, McLeod L, Hayward RC, Hull T, Santangelo CD, et al. Using origami
 1110 design principles to fold reprogrammable mechanical metamaterials. *Science* **345** (2014) 647–650.
- 1111 [123] Liu K, Paulino GH. Nonlinear mechanics of non-rigid origami: an efficient computational approach.
 1112 *Proc. Roy. Soc. A* **473** (2017) 1–28.